HHS Public Access

Author manuscript

Science. Author manuscript; available in PMC 2026 June 25.

Published in final edited form as:

Science. 2026 March 05; 391(6789): eads3972. doi:10.1126/science.ads3972.

Targeting amyloid-β pathology by chimeric antigen receptor astrocyte (CARA) therapy

Yun Chen[1,2,†], **Yizhou Liu**[2,†], **Khai Nguyen**[2,†], **Junjie Wu**[2], **Sihui Song**[1], **Kent Lin**[2], **Patrick F. Rodrigues**[2], **Siling Du**[2], **Charles Zhou**[1], **Kyle Xiong**[2], **Megan Bosch**[1], **Peter Bor-Chian Lin**[1], **Darya Khantakova**[2], **Shitong Wu**[2], **May Wu**[2], **Carla Yuede**[1], **David M. Holtzman**[1,3,4], **Marco Colonna**[2,3,5,*]

[1]Department of Neurology, Washington University School of Medicine, St. Louis, MO 63110, USA

[2]Department of Pathology and Immunology, Washington University School of Medicine, St. Louis, MO 63110, USA

[3]Hope Center for Neurological Disorders, Washington University School of Medicine, St. Louis, MO 63110, USA

[4]Knight Alzheimer's Disease Research Center, Washington University School of Medicine, St. Louis, MO 63110, USA

[5]Center for Brain Immunology and Glia (BIG), Washington University in St. Louis, School of Medicine, St. Louis, MO, USA

Abstract

Alzheimer's disease (AD) is the leading cause of dementia and is characterized by progressive amyloid accumulation followed by tau-mediated neurodegeneration. Despite advances in anti-amyloid immunotherapies, important limitations remain, highlighting the need for new therapeutic strategies. Here, we introduce anti-amyloid chimeric antigen receptors expressed in astrocytes (CAR-A) and validate their function *in vitro*. We show that two CAR-A designs reduce amyloid and associated pathology after plaque formation and prevent early plaque deposition *in vivo*. Single-nucleus RNA sequencing shows that CAR-A treatment induces a distinct glial response to amyloid pathology involving coordinated activity of astrocytes and microglia. Each construct additionally elicits unique, receptor-specific effects in astrocytes or microglia. Together, these findings support the therapeutic potential of CAR-expressing astrocytes as a disease-modifying strategy for AD.

[*]Correspondence: Marco Colonna, mcolonna@wustl.edu.
[†]These authors contributed equally.

Author contributions:
Conceptualization: YC, MC
Methodology: YC, YL, KN, CY, MC
Investigation: YC, YL, KN, JW, SS, KL, PR, SD, CZ, KX, MB, PBL, DK, SW, MW, CY
Visualization: YC, YL, MC
Funding acquisition: MC
Supervision: MC, DMH
Writing – original draft: YC, MC
Writing – review & editing: YC, YL, DMH, MC

Introduction

Alzheimer's disease (AD) is the most common cause of dementia worldwide, with rising prevalence due to an aging population (1). AD follows a distinctive pathological cascade: amyloid-β (Aβ) deposits accumulate in the extracellular space, leading to the hyperphosphorylation of intraneuronal tau proteins, eventually forming tau-associated paired helical filaments that are closely linked with substantial neurodegeneration (2, 3). Although the amyloid cascade theory's ability to fully explain AD is debated (4–6), the latest generation of anti-Aβ monoclonal antibodies (mAbs), such as Lecanemab and Donanemab, has shown promising results. Anti-Aβ mAbs primarily function through antibody-dependent cellular phagocytosis (ADCP) (7), clearing Aβ aggregates via microglia-mediated clearance. Both Lecanemab and Donanemab have received FDA approval, supporting the effectiveness of anti-Aβ therapies in slowing the progression of AD. In addition, the DIAN-TU trial recently showed promising results in long-term treatment to reduce disease risk in the autosomal dominant AD patients (8). However, these treatments require very high doses of mAbs to achieve sufficient penetration into the central nervous system (CNS), raising concerns about the high cost of long-term therapy (9–11). Furthermore, the potential side effects necessitate frequent monitoring of patients receiving these antibodies, complicating their clinical use (5, 12, 13). Current mAb treatments carry potential side effects including amyloid-related imaging abnormalities (ARIA). Another challenge is determining the optimal treatment window (14). Early intervention to remove amyloid deposits may prevent AD progression (15–17), whereas delayed treatment at more advanced disease stages may not consistently produce meaningful improvements in slowing cognitive decline (18, 19). Moreover, anti-Aβ mAb-based therapies rely on ADCP via FcRγ signaling, which limits the flexibility to fine-tune cellular responses (20). Therefore, there is an urgent need for new therapeutic approaches that offer improved efficacy, safety, convenience and flexibility for AD treatment.

To address these challenges, we propose a paradigm shift in a method to remove Aβ deposits through the development of chimeric antigen receptors (CARs). By engineering CARs that combine an anti-Aβ single-chain variable fragment (scFv) with the intracellular domain of certain phagocytic receptors, we can create a self-sustaining therapeutic system within the brain's cellular milieu. This innovative approach circumvents the need for repeated interventions, offering potential one-time treatment that could provide sustained therapeutic action throughout the course of disease. Additionally, unlike antibodies, CARs can be engineered to trigger specific intracellular signaling pathways, allowing precise control over cellular responses. This strategy allows for highly targeted, customizable interventions for AD, including during the critical window for secondary prevention following anti-Aβ mAb treatment.

The CAR approach has been pioneered in cancer immunology (21, 22), where CARs specific for tumor antigens have been designed and primarily deployed in T cells (23, 24). More recently, phagocytic CARs specific to tumor antigens have also been implemented in monocytes/macrophages (25, 26). Preliminary studies recently also showed successful *in vitro* targeting of Aβ aggregates by FcRγ-based designs expressed in myeloid cells (27, 28). However, due to the tightness of the blood-brain barrier and the self-sustaining

nature of microglia already residing in the CNS, efficient methods to replace microglia with engineered peripheral monocytes or other myeloid cells are still in development (29–33). Moreover, the survival of engineered myeloid cells in the face of massive amyloid deposition in the brain remains a challenge. For example, an Fcγ receptor-based CAR macrophage injected intracranially into the hippocampus has shown limited survival and therapeutic effects in removing amyloid pathology *in vivo* (27). Direct viral infection to engineer endogenous microglia through noninvasive gene delivery approaches is also in its preliminary stages (34–36). To date, there is no conclusive evidence that CAR myeloid cells can exert a sustained effect in mitigating AD-related pathology *in vivo*.

In this study, we explored whether another type of phagocytic glial cell, the astrocyte (37–39), could be leveraged to overcome the challenges mentioned above. Astrocytes contribute to the clearance of Aβ aggregates, complementing microglial responses to amyloid pathology (40–42). We introduced anti-Aβ CARs into astrocytes using the Adeno-associated virus (AAV), creating CAR-expressing astrocytes (CAR-A) that could act as super-phagocytes, specifically targeting and removing extracellular Aβ aggregates. We designed CAR-As independent from FcRγ signaling that boosted astrocytic phagocytosis of Aβ oligomers *in vitro*. Additionally, we delivered two of these CARs into CNS astrocytes *in vivo* through peripheral noninvasive gene delivery using the AAV-PHP.eB strain with a GFAP-promoter (43, 44). This approach resulted in a substantial reduction in amyloid pathology *in vivo*. We also demonstrated that a single administration of either CAR-A therapy before Aβ deposition in the 5xFAD mouse model prevented amyloid accumulation and associated pathology. Additionally, single-nucleus RNA sequencing (snRNAseq) revealed that both CAR-A treatments activated astrocytes and promoted a microglial profile consistent with reduced exhaustion, with minor differences in the specific patterns of astrocyte and microglial activation. Overall, our results demonstrate the effectiveness of the anti-Aβ CAR-A concept and highlight the therapeutic potential of CAR-A for decreasing Aβ deposition and treating AD.

Construct development for anti-Aβ CARs

In the CNS, microglia and astrocytes act as phagocytes equipped with receptors and downstream signaling capable of directly engulfing cells, synapses, particles, or debris (45–48). Additionally, microglia can phagocytose cells or particles that are coated with antibodies through Fc receptors (49). To develop functional anti-Aβ CARs, fusion proteins must be designed that integrate effectively into the pre-existing signaling networks of the target cells (Figure 1A). Thus, we decided to leverage receptors intrinsically expressed in the CNS phagocytes and capable of direct phagocytosis. We linked an anti-Aβ scFv to the intracellular domain of one of three receptors that mediate phagocytosis in development, homeostasis and disease of the CNS: MEGF10, expressed by astrocytes (50); Dectin1 (also known as CLEC7A), expressed by microglia (51); and MERTK, expressed by both (50, 52). In one additional CAR, we linked the anti-Aβ scFv to the signaling domain of CD3ζ, which is well-established for CAR-T signaling (53). This CD3ζ construct shares homology with the Fc common γ-chain, FcεRIγ, a key signaling molecule mediating ADCP in macrophages and microglia, which has been deployed to design an anti-tumor CAR macrophage with success (22). We mirrored the Dectin1 intracellular sequence from C-

terminal to N-terminal due to its type II transmembrane receptor feature (54). We connected the anti-Aβ scFv and each intracellular domain with the transmembrane domain of CD8 adopted from CAR-T constructs with one exception: since the scFv-CD8-MERTK chimeric construct was not efficiently expressed, we replaced the CD8 transmembrane region with that of endogenous MERTK transmembrane sequence (Figure 1A). For the initial *in vitro* screening, we derived the anti-Aβ scFv from the sequence of Crenezumab (Crene) due to the availability of its structure in complex with the Aβ42 peptide (55). On the basis of this X-ray crystal structure, we designed a suitable $(GGGGS)_4$ linker from the C-terminal of the heavy chain to the N-terminal of the light chain to maintain antigen binding ability. We also tagged all CAR constructs with a bright GFP (GreenLantern) at the C-terminal and cloned them into a lentiviral vector for transduction.

As a preliminary screen of CAR constructs' function, we expressed all constructs in an SV40T-immortalized mouse astrocyte cell line (imA) to validate their surface expression (Figure 1B) and functional capacity (Figure S1A–E) in astrocytes. We confirmed Aβ surface binding by incubating CAR-imAs with monomeric Aβ42 labeled with the stable dye AlexaFluor-647 (A647) on ice, followed by flow cytometry; we observed no binding in GFP-expressing imAs (Figure S1A). To assess phagocytic function, we oligomerized Aβ42 conjugated with the pH-sensitive dye pHrodo (oAβ42) and incubated CAR-imAs and GFP-imAs with oAβ42-pHrodo at 37°C. After 4 hours, CAR-imAs exhibited clear uptake compared to controls, with most cells showing low uptake and a smaller subset showing high uptake. By 24 hours, the pHrodo signal had largely decayed in low-uptake cells but remained in high-uptake cells (Figure S1B–C). We observed similar results using oAβ42 conjugated to A647: following a 4-hour pulse, CAR-imAs internalized oAβ42 and showed a marked reduction in intracellular A647 signal by 24 hours, consistent with degradation of internalized aggregates (Figure S1D–E). Lastly, to confirm the target specificity of CAR-A scFvs, we employed a dual-challenge assay in which CAR-imAs were simultaneously exposed to oAβ42 and a second pHrodo-labeled substrate (Figure S1F). These substrates included disease-relevant biomolecules and aggregates such as tau extracts from AD brains (AD-tau), recombinant tau fibrils, α-synuclein pre-formed fibrils (PFFs), and myelin debris. CAR-imAs did not increase uptake of AD-tau, tau fibrils, α-synuclein, or myelin in the presence of oAβ42 (Figure S1G), unlike the GFP controls, which exhibited enhanced AD-tau uptake with oAβ42. These results indicate that CAR-induced phagocytosis is antigen-specific, driven by the scFv domain, rather than a generalized response to antigen exposure.

Functional verification for anti-Aβ CAR in astrocytes

Next, we validated the functionality of all four CAR constructs on commercially sourced primary astrocytes. We transduced these cells with the same lentivirus constructs and challenged them with oAβ42-A647 (Figure 1C–D). Although primary astrocytes required more time to internalize Aβ42 aggregates—approximately 8 hours compared to 4 hours in immortalized cells—and showed slower degradation, occurring over 72 hours versus 24 hours, CAR-As consistently enhanced phagocytosis of oAβ42 followed by degradation (Figure 1C–D). Thus, all four CAR designs showed comparable ability to phagocytose and digest oAβ42. Although CD3ζ and Dectin-1 are not normally expressed in astrocytes, their intracellular domains may couple to alternative signaling partners to promote phagocytosis.

For subsequent experiments, we focused on CARs incorporating phagocytic signaling domains from Megf10, a native astrocytic engulfment receptor, and from Dectin-1, a non-astrocytic phagocytic receptor chosen to test whether alternative phagocytic pathways can be harnessed for Aβ clearance.

Previous clinical trials showed that the efficacy of anti-Aβ monoclonal antibodies in clearing plaques depended on their ability to preferentially bind fibrillar rather than soluble Aβ, given the sink effect of abundant soluble Aβ (56). Based on this, we surveyed different scFv components for Megf10- and Dectin1-CARs to optimize their application *in vivo* in both a preventive and therapeutic approach. We selected two scFvs: Crenezumab, which recognizes both soluble Aβ monomers and oligomers, and Aducanumab, which preferentially binds Aβ oligomers—including early forms—without targeting soluble Aβ monomers (55, 57, 58). For the latter, we designed to translate Aducanumab scFv from light chain to heavy chain to avoid potential interference of antigen binding (59). To validate these constructs, we transduced primary astrocytes with lentiviruses encoding Crene-Megf10, Adu-Megf10, Crene-Dectin1 or Adu-Dectin1 and then challenged them with oligomeric Aβ42-pHrodo (Figure 1E–G). Crene-Megf10 expression led to a greater increase in astrocytic Aβ phagocytosis than the other CAR designs, whereas Crene-Dectin1 and Adu-Dectin1 showed similar increase in Aβ phagocytosis (Figure 1G). Additionally, because the full-length Megf10 intracellular domain was too large for AAV packaging, we tested a truncated version that retained the essential endocytosis domain. This shortened construct maintained similar phagocytic activity (Figure S1H–J). Based on these data, we prioritized two CAR constructs —Crene-Megf10 and Adu-Dectin1—for *in vivo* evaluation. This selection balanced strong *in vitro* performance with design diversity—incorporating distinct scFv specificities and intracellular signaling domains—to maximize the chance of identifying design principles that drive efficacy in the CNS and to help de-risk future translational development.

To achieve efficient brain penetration and expression of CARs in astrocytes *in vivo*, we cloned Crene-Megf10, Adu-Dectin1 CARs and a GFP control into a GFAP-promoter-based AAV-PHP.eB expression system (44, 60) (Figure S2A). We also replaced the CD8α transmembrane peptide with rat CD8α homolog sequence to avoid potential co-receptor binding (61). Inserting the Crene-Megf10 CAR into the AAV vector required using a shorter version of the GFAP promoter (GfaABC1D) due to size constraints (62). First, we tested the two AAV-PHP.eB.GFAP-CAR constructs in primary astrocytes from mixed glial cultures derived from P3–5 cortex to assess uptake and degradation of oAβ42 (Figure S2B). We gated astrocytes and microglia as $CD11b^{-}$ and $CD11b^{+}$ cells, respectively (Figure S2C). Although both CAR-A constructs increased Aβ42 uptake by astrocytes compared to the GFP control, Crene-Megf10 CAR-A showed a more pronounced enhancement (Figure 1H–K). Adu-Dectin1 CAR-A also enhanced microglial uptake of oAβ42 ($CD11b^{+}$ gated, Figure 1L–M), suggesting that astrocytes may influence microglia through cell-surface ligands or soluble factors.

We next assessed the *in vivo* phagocytic potential of CAR-As in WT mice. We firstly injected AAV-PHP.eB-CARs intravenously via the retro-orbital sinus. One month later, we injected pre-labeled Aβ42-A647 fibrils into the mice intracerebrally (Figure S3A). Three days after fibril injection, we isolated hippocampi and analyzed GFP^{+} cells by flow

cytometry for Aβ42-A647 content. Results showed an increased uptake of Aβ42-A647 by GFP^+ astrocytes expressing the Adu-Dectin1 CAR-A construct compared to the GFP control (Figure S3B–E). We further examined the durability of GFP expression in 6-month-old 5xFAD males at 1, 2, and 3 months post-AAV injection (Figure S3F). Whereas the GFP control showed the highest fluorescence, both Crene-Megf10 and Adu-Dectin1 CAR-As maintained stable expression in the CNS over the three-month period. Astrocytes expressing either CARs remained clustered around X34-labeled amyloid plaques at 3 months post-infection (Figure S3G). These results supported advancing both Crene-Megf10 and Adu-Dectin1 CAR-As to large *in vivo* cohorts.

Late timepoint CAR-A treatment reduces Aβ pathology *in vivo*

To determine the therapeutic potential of AAV-PHP.eB-expressing CAR-As, we administered them intravenously in a cohort of age- and sex-matched 5xFAD mice at 6 months of age and waited for 3 months to assess the amyloid pathology when amyloid plaque formation has reached a plateau according to previous literature (63, 64) (Figure 2A). At 9 months of age, we assessed amyloid burden across the hemibrain using X34 staining of Aβ plaques on two brain sections per mouse. Both AAV-PHP.eB-Crene-Megf10 and AAV-PHP.eB-Adu-Dectin1 CAR-A treatments led to an overall ~50% decrease in total amyloid load after a single injection (Figure 2B–C), with a similarly marked reduction in Aβ plaques in both cortex and hippocampus compared to controls (Figure 2D–F). ELISA analysis of cortical fractions confirmed reductions in insoluble Aβ42 aggregates in both CAR-treated groups (Figure 2G). Insoluble Aβ40 and soluble Aβ42 and Aβ40 amounts remained unchanged in both CAR-treated groups, except for an increase in soluble Aβ40 in the Crene-Megf10–treated group compared to the GFP control (Figure 2H).

To evaluate neuronal changes, we stained for LAMP1 to assess plaque-associated neuritic dystrophy in cortex and hippocampus (Figure 2I–K). Consistent with reduced amyloid deposition, both CAR-A treatments substantially decreased the volume of dystrophic neurites surrounding $X34^+$ plaques (Figure 2I–K). We further examined pre- and post-synaptic loss by staining for Synapsin and PSD95, respectively. Crene-Megf10 treatment alleviated post-synaptic loss, whereas we observed no rescue in synaptic loss in the Adu-Dectin1 group (Figure 2L–O). In summary, a single dose of AAV-PHP.eB-delivered CAR-A therapy reduced amyloid burden and neuronal dystrophy *in vivo*, with partial rescue of synaptic integrity in the Crene-Megf10–treated group.

Early timepoint CAR-A intervention prevents amyloid accumulation

Recently, the DIAN-TU project launched the primary prevention trial to evaluate whether early removal of amyloid plaques in patients with autosomal dominant AD can influence their risk of AD development (16). Aligning with this concept of early intervention, we explored the potential of our two CAR-A therapies as a preventive strategy. We injected the viruses intravenously at 2.5 months instead of 6 months of age in 5xFAD mice, before they exhibit Aβ plaques (63) (Figure 3A). Then we examined all mice at 5 months of age, when early Aβ plaques had formed. We first assessed overall amyloid load across the hemibrain using X34 staining of Aβ plaques. AAV-PHP.eB-Crene-Megf10

and AAV-PHP.eB-Adu-Dectin1 treatments reduced amyloid plaque formation 2.5 months post-injection compared to AAV-PHP.eB-GFP (Figure 3B–C), with the Crene-Megf10 group showing almost no amyloid plaques. In both cortex and hippocampus, AAV-PHP.eB-Crene-Megf10 and AAV-PHP.eB-Adu-Dectin1 treatments led to a similar reduction in Aβ plaques compared to controls (Figure 3D–F). ELISA analysis revealed that Aβ42 amounts in the PBS-insoluble but GdnHCl-soluble fraction were reduced in both CAR-A–treated groups compared to controls, with undetectable amounts in the Crene-Megf10 group (Figure 3G). In contrast, we observed no differences in Aβ40/42 amounts in the PBS-soluble fraction between CAR-treated groups and controls (Figure 3H). We also assessed neuronal dystrophy around residual plaques in the cortex and hippocampus using LAMP1 staining (Figure 3I–K). Due to the substantial reduction in Aβ plaques in the AAV-PHP.eB-Crene-Megf10 and AAV-PHP.eB-Adu-Dectin1 groups, we analyzed only three plaques per hippocampal section (2 sections per mouse) (Figure 3I–K). Consistent with the overall reduction in amyloid burden, both CAR-treated groups showed a decrease in the volume of dystrophic neurites surrounding $X34^+$ plaques compared to controls (Figure 3I–K). At this disease stage, both CAR treatments also alleviated plaque-associated synaptic loss, as evidenced by improved Synapsin and PSD95 staining (Figure 3L–O). Overall, our findings show that early administration of either AAV-PHP.eB-Crene-Megf10 or AAV-PHP.eB-Adu-Dectin1 at 2.5 months of age in the 5xFAD model can substantially reduce amyloid pathology, as well as associated neuronal dystrophy and synaptic loss.

Limited behavioral improvement upon CAR-A treatments

Since behavioral deficits have been reported in the 5xFAD model—though inconsistently across studies (65, 66)—we assessed whether CAR-A treatment could improve cognitive function. In the 9-month cohort, treatment with CAR-As, particularly Adu-Dectin1, reduced overall activity (Figure S4A–G), but we did not find other behavioral differences (Figure S4B–C). At 5 months, we did not observe behavioral differences. Thus, despite a marked reduction in amyloid pathology, CAR-A treatment did not result in improvements in memory-related behaviors at either 5 or 9 months of age. A safety assessment in wild-type mice revealed mild but detectable alterations following AAV-PHP.eB administration, including increased center zone time in motor function tests and total entries in the elevated plus maze compared to PBS controls, which may confound the performance in cognitive tests (Figure S4I–K). In addition, the increased phagocytic activity induced by AAV-PHP.eB–Crene-Megf10 or AAV-PHP.eB–Adu-Dectin1 may inadvertently promote synapse pruning, potentially offsetting the beneficial effects of amyloid clearance. Accordingly, translating CAR-A–mediated pathological improvement into functional recovery will likely require further optimization of CAR design to better preserve circuit integrity (67). Finally, broader behavioral testing will be important, given reported variability and known limitations of the 5xFAD model (65, 66).

CAR-A treatments induce unique glial cell responses

Given the rescue of peri-plaque neuronal dystrophy in both Crene-Megf10 and Adu-Dectin1 CAR-A treatments (Figures 2–3), we investigated whether CAR-A-mediated Aβ clearance influences peri-plaque glial responses *in vivo* (68, 69). To this end, we analyzed the

distribution, morphology, and activation states of astrocytes and microglia surrounding $X34^+$ Aβ plaques using confocal microscopy (68–72). At 9 months, Crene-Megf10–treated mice showed a modest increase in astrogliosis (total % of $GFAP^+$ volume/Z-stack volume) and astrocyte clustering around plaques compared to the GFP control (Figure 4A–C, S5A–C), whereas Adu-Dectin1 treatment resulted in no differences relative to GFP. At 5 months, however, Adu-Dectin1 induced greater astrogliosis and astrocyte clustering around plaques than the GFP control, whereas Crene-Megf10 had no effect (Figure 4D–F, S5D–F).

At 9 months, Adu-Dectin1 treatment led to greater microglial clustering around plaques, whereas both CAR-A therapies reduced overall microgliosis (total % of $IBA1^+$ volume/Z-stack volume) in the cortex and hippocampus, likely reflecting the reduced Aβ burden (Figure 4G–I, S5G–I). At 5 months, despite the overall low plaque burden, Adu-Dectin1-treated mice showed increased microglial clustering around the few existing plaques in the ventral retrosplenial cortex. Together, these findings suggest that Aβ clearance by CAR-As influences local glial responses in a construct- and age-dependent manner, with Crene-Megf10 primarily enhancing astrocytic response around plaques, whereas Adu-Dectin1 promotes some microglial clustering, particularly at earlier stages. This observation is consistent with moderate differences in astrocyte vs. microglia phagocytosis in the mixed glial culture (Figure 1I–N).

To further characterize glial responses to CAR-A treatment, we performed snRNA-seq on pooled brain samples from five mice per group. Groups included Crene-Megf10, Adu-Dectin1, and GFP controls at both 5 and 9 months of age. Initial clustering of all nuclei identified all major CNS cell populations after removing most neuronal nuclei, with an overrepresentation of oligodendrocytes (Figure S6A–B), and confirmed effective AAV-PHP.eB delivery to astrocytes, as indicated by high expression of Woodchuck hepatitis virus Post-transcriptional Regulatory Element (WPRE) specifically in this population (Figure S6C–D). Oligodendrocytes and OPCs from Crene-Megf10- and Adu-Dectin1-treated mice showed minimal transcriptional changes, aside from reduced expression of the activation marker *C4b* in Crene-Megf10–treated 5-month mice, consistent with the low plaque burden (Figures S6E–H).

Since astrocytes and microglia were initially underrepresented (Figures S6I–J), we performed nuclear sorting to deplete oligodendrocyte nuclei from hippocampal samples, resulting in substantial enrichment of astrocyte and microglial nuclei for deeper analysis (Figure S7A–C). In the enriched dataset, we first focused on astrocytes. Both CAR-A treatments upregulated astrocytic DEGs including *Lrp1b*, *Gfap*, *Cxcl5*, *Clu*, and *S100a6* (9 months), *Cdh19* and *Zbtb16* (5 months), while downregulating *Fam163a*, *Cmss1*, and *Il31ra* (9 months) and *Zfp949* (5 months) (Figure S7D–E). Pathway analysis revealed that these transcriptional changes were associated with astrocyte development, neurogenesis, neuron projection formation, and cell–cell signaling. Crene-Megf10 preferentially upregulated genes involved in astrocyte differentiation and lipid metabolism (Figure S7F). Analysis of microglial DEG revealed that both CAR-A treatments were associated with microglial activation markers (*Cst3*, *Apoe*, *Trem2*, *C1q*), whereas Adu-Dectin1 was also associated with increased MHC genes (*Cd74*, *H2-Aa*, *H2-D1*) (Figure S7G–H). Pathway analysis confirmed upregulation of antigen processing, presentation, and endocytosis pathways,

with these microglial responses more pronounced at 9 months—consistent with the greater amyloid burden at this stage (Figure S8I). Almost no DEGs were detected in OPCs (Figure S7J–K).

To obtain a more granular view of astrocytes, we re-clustered astrocytes into known subtypes—homeostatic, transitional (TA1, TA2), disease-associated astrocytes (DAAs), and MyoC$^+$ astrocytes—based on published markers (73) (Figure 5A–B, S8A). We validated our DAA and MyoC clusters by mapping onto reference snRNA-seq UMAPs, showing strong alignment with known astrocyte trajectories (Figure 5C). 2D and 3D trajectory analyses revealed two distinct lineages: one progressing through TA1 towards DAAs, and another via TA2 towards MyoC$^+$ astrocytes (Figure 5D). Pathway analysis showed that DAAs upregulated phagocytic and lysosomal genes, whereas MyoC$^+$ astrocytes were enriched for synaptic and metabolic pathways (Figure S8B).

Analysis of the relative abundance of astrocyte populations across treatments showed that both CAR-As expanded DAAs and reduced TA1 at 9 months (Figure 5E, S8C). Only Crene-Megf10 increased TA2 and MyoC$^+$ astrocytes. RNA velocity analysis revealed uniform transitions toward both terminal states in Crene-Megf10, whereas Adu-Dectin1 astrocytes proceeded towards DAA following a nonlinear path (Figure 5F). Pseudotime analysis confirmed that both CAR-As expanded DAAs, whereas only Crene-Megf10 treatment also triggered a TA2-dependent trajectory toward MyoC$^+$ astrocytes (Figure 5G–H). At 5 months, these trajectories were absent likely due to lower pathology, except for a modest increase of MyoC$^+$ astrocytes in Crene-Megf10 treated animals (Figure S8D–E).

We next used explained DEG analysis to determine which clusters contributed most to gene expression changes (Figure 5I–J). In Crene-Megf10-treated mice, the DAA and MyoC$^+$ astrocytes primarily accounted for upregulated genes (Figure 5I), whereas in Adu-Dectin1-treated mice, DEG were largely restricted to DAAs (Figure 5J). Despite a substantial overlap in the overall DEG sets, Crene-Megf10 treatment induced DAA- and MyoC$^+$ astrocytes-related genes, whereas Adu-Dectin1 treatment upregulated genes associated with DAAs (Figure 5K). At 5 months, Crene-Megf10 treated animals showed the highest module score upregulation in TA1 astrocytes (Figure S8F), suggesting that induction of DAA and MyoC$^+$ astrocytes represents a later-stage response emerging as amyloid burden increases. Accordingly, DEGs alignment showed no differential induction of DAA vs. MyoC$^+$ astrocytes between Crene-Megf10 and Adu-Dectin1 treatments at 5 months (Figure S8G).

To validate the impact of Crene-Megf10 or Adu-Dectin1 treatment on astrocytic activation compared to controls in response to amyloid burden at 9 months, we chose LRP1 as a marker of reactive astrocytes, including DAA and MyoC$^+$ populations (Figure S8H). We performed immunofluorescence staining for LRP1 in GFAP$^+$ astrocytes and quantified its expression around X34$^+$ plaques. We observed an increase of astrocytic LRP1 in Crene-Megf10–treated mice but not in Adu-Dectin1–treated animals (Fig. 5L–M), consistent with enhanced astrocytic engagement with plaques, as indicated by X34$^+$ Aβ colocalization with lysosomes in plaque-associated astrocytes (Fig. S8I).

To further explore potential astrocyte–microglia cross-talk, we conducted ligand–receptor pairs analysis using NicheNet, focusing on astrocytic ligands and microglial receptors (Figure 5N–O). At 9 months, both treatments promoted a shared communication network involving 18 astrocytic ligands—such as *Vcam1*, *Sdc2*, *Sema4a/b*, *Lrp1b*, *Gpc6*, *Clu*, and *C4b*—paired with 17 microglial receptors, including *Trem2/Tyrobp*, *Itga5*, *Itga9*, *Lrp5*, and *C5ar2* (Figure 5P–Q). We also detected a subset of these interactions in the 5 months cohort (Figure S8J–K). In Crene-Megf10 treated mice, *Apoe* and *Adam23* were selectively upregulated in astrocytes, whereas *Adam10/17* were enriched in microglia. In Adu-Dectin1 treated mice, *Cd74*, *Notch2*, and *Itga4/6* were prominent in microglia (Figure 5P–Q). These findings suggest that two CAR-A constructs not only enhance Aβ clearance but also distinctly modulate glial communication and downstream signaling pathways to varying extents.

To determine the indirect effects of CAR-A treatment on microglia, we re-clustered microglial nuclei into subtypes corresponding to established signatures: homeostatic, transitional, DAM1, DAM2, cycling, IFN-responsive, and MHC-expressing microglia (Figure 6A–B) (74, 75). Notably, we identified a distinct microglia subset that co-expressed DAM genes (such as *Apoe*, *Trem2* and *Cd68*) together with homeostatic markers (*Hexb*, *Csf1r*), defining a hybrid state that was clearly separable from classical DAM or MHC clusters (Figure 6B, S9A). UMAP projection of published DAM gene sets (76) confirmed their partial overlap with this unique population (Figure S9B). We refer to this subset as the $CSF1R^{high}/CD68^{high}$ microglia. At 9 months, both CAR-A treatments increased the $CSF1R^{high}/CD68^{high}$ population and reduced DAM1 and DAM2 clusters (Figure 6C, S9C–D). Additionally, we observed expansion of MHC-II-expressing microglia only in the Adu-Dectin1 treatment group (Figure 6C–D). Consistent with this, explained DEG analysis showed that, in Adu-Dectin1-treated mice, $CSF1R^{high}/CD68^{high}$ and MHC-II clusters accounted for the majority of the transcriptional changes (Figure S9E–F). Both CAR-A treatments were associated with reduced DAM1 and DAM2 signatures compared to the GFP control (Figure 6E). In 5-month mice, in which amyloid burden was low, we observed more homeostatic microglia and fewer $CSF1R^{high}/CD68^{high}$ cells (Figure S9C–D), with minimal changes in other activated subtypes.

Immunofluorescence validated the microglia snRNAseq profiles. In untreated 5xFAD mice, peri-plaque microglia showed the expected $CSF1R^{low}/CD68^{high}$ DAM phenotype. In contrast, in both CAR-A–treated groups, microglia surrounding plaques displayed a $CSF1R^{high}/CD68^{high}$ phenotype (Figure 6F–G), with a marked enrichment of this population around $X34^{+}$ plaques (Figure 6G). This phenotypic shift was associated with increased $CD68^{+}$ voxels in plaque-associated $IBA1^{+}$ microglia, especially in the Adu-Dectin1 group, in which $X34^{+}$ Aβ aggregates were frequently observed in microglia lysosomes (Figure 6H–I, Fig. S9G and S10A–B). Consistent with reduced classical DAM activation, both CAR-treated groups downregulated GPNMB—a DAM2 marker—in plaque-associated microglia (Figure 6J–K, S10C–D). Further, immunostaining and quantification revealed an increase in $MHC\text{-}II^{+}/IBA1^{+}$ microglia specifically in the Adu-Dectin1 treatment group (Figure 6L–M, S10E–F), whereas no such increase was observed with Crene-Megf10 treatment. Similarly, Clec7A (Dectin1)—a marker shared by DAM2 and MHC populations—was elevated in the cortex and hippocampus of Adu-Dectin1-treated mice (Figure S10G–H), consistent with

transcriptomic data showing *Clec7a* enrichment in both DAM and MHC clusters (Figure 6B). In summary, both CAR-A treatments promoted a CSF1R^{high}/CD68^{high} microglial state, while reducing the DAM2 state. Given the association of the CSF1R^{high}/CD68^{high} profile with lower amyloid burden, this shift may reflect decreased stress and exhaustion of microglia secondary to reduced amyloid load.

Discussion

In this study, we show that two selected CARs—Crene-Megf10 and Adu-Dectin1—effectively reduced amyloid burden *in vivo*. These constructs, chosen from four designs based on phagocytic receptors, operate independently of classical FcRγ signaling, which underlies ADCP by mAbs. Given the established role of astrocytes as phagocytes in both health and disease (38, 39, 48, 50, 77), and their numerical abundance over microglia, we targeted these CARs to astrocytes using the CNS-penetrant AAV-PHP.eB vector, enabling non-invasive delivery. Astrocytic CAR expression offers several advantages: 1. It reduces the Aβ burden on microglia, as shown by their increased CSF1R^{high}/CD68^{high} profile and reduction in DAM gene signatures. 2. It avoids complications related to peripheral immune cell infiltration seen in microglia replacement strategies (3, 31, 32, 78). 3. It allows efficient and durable *in vivo* delivery without intracranial injection (43, 79).

A single AAV injection led to sustained CAR expression in astrocytes for at least three months and decreased plaque load. Early intervention—before plaque formation—achieved greater amyloid prevention, suggesting the potential for a one-time, disease-modifying treatment. Although the AAV-PHP.eB platform is widely used and over 100 active clinical trials are using AAV therapies for neurological disorders (80), including trials in AD (NCT05040217, NCT00876863), we did observe altered motor activity in treated animals, which may have contributed to—or confounded—the lack of behavioral rescue. This aligns with reports of side effects in some AAV-based clinical trials (80–82) and underscores the need for safer delivery platforms such as optimized AAV, lipid nanoparticles or RNA-based systems. Although we did not notice peripheral effects such as in the spinal cord or gut, potential off-target effects of AAV in peripheral GFAP^{+} glial cells should also be evaluated in future studies.

snRNA-seq and immunostaining showed that both CARs induced DAAs. Although DAAs were once considered detrimental (73), our data suggest they may play a protective role in this context, supported by upregulation of LRP1 in plaque-associated astrocytes, a known mediator of Aβ clearance (83). Both CAR-A treatments were also associated with changes in microglial responses, leading to the emergence of a CSF1R^{high}/CD68^{high} microglial population. This cluster retained homeostatic genes (such as *Csf1r*, *Hexb*) alongside DAM markers (*Trem2*, *Apoe*), an intermediate activation state that diverges from canonical DAM1/2 programs, perhaps reflecting reduced microglial stress and exhaustion due to lower Aβ load contributed by CAR-A treatments. Immunostaining confirmed that this population replaced classical CSF1R^{low}/CD68^{high} and GPNMB^{+} DAM microglia near plaques in CAR-treated animals.

Some nuances were observed between Crene-Megf10 and Adu-Dectin1 CAR-A treatments. In early-intervention cohorts, Crene-Megf10 more effectively limited plaque formation, possibly reflecting its broader binding profile, as Crenezumab recognizes both soluble and oligomeric Aβ species. In late treatment cohorts, Crene-Megf10 also increased a $MyoC^{+}$ astrocyte population associated with differentiation and lipid metabolism. In contrast, Adu-Dectin1 induced stronger microglial clustering, activation, and phagocytic activity, supported by in vitro assays and by increased expression of MHC-II and Clec7A in vivo at later time points. Together, these results indicate that astrocyte-mediated Aβ clearance by CAR-As shapes glial responses in a construct-specific and stage-dependent manner. Some differences may reflect the specific Aβ species recognized by each scFv, whereas others may arise from distinct intracellular signaling pathways engaged by the CAR constructs, which can influence expression of cell-surface molecules and soluble mediators that shape microglial interactions. Regardless, astrocytes equipped with CARs can effectively clear amyloid pathology through phagocytosis, even when built with anti-Aβ antibodies previously shown to have limited clinical efficacy. Compared to CAR-microglia or CAR-macrophages, which face challenges in engraftment and delivery (27) (29–32), astrocyte-targeted CARs delivered via AAV-PHP.eB provide a promising and scalable alternative.

Astrocytes are known to play essential roles in regulating neuronal activity (84) and, like microglia, may contribute to synaptic pruning through their phagocytic function (85, 86). However, due to limitations of the current disease model, it remains unclear whether direct manipulation of astrocytes using our CAR system could lead to adverse effects from enhanced phagocytic activity. Despite clear reductions in amyloid pathology, behavioral outcomes—particularly in the late-stage Adu-Dectin1 cohort—did not show corresponding improvement. It remains unclear whether signaling from CAR intracellular domains, especially Dectin-1, further amplifies activation of amyloid-primed glia, thereby disrupting synapse maintenance and neuronal function and offsetting the benefits of plaque reduction. Consistent with this possibility, CAR-A treatment in this cohort failed to rescue amyloid-associated synapse loss to the same extent observed in the early-intervention group. Together, these findings indicate that optimization of CAR-A signaling design, dosing strategies, and treatment timing will be essential to achieve cognitive benefit and underscore the need for systematic evaluation of potential side effects across multiple disease models and with more comprehensive behavioral testing. Future work should also assess how CAR-A compares with other gene- and cell-based approaches and whether combination strategies, including astrocyte-targeted metabolic therapies, can further enhance functional recovery (87). This work provides a foundation for extending phagocytic CAR approaches in astrocytes or other cell types to other neurodegenerative diseases involving protein aggregates, such as Tau in AD, with the potential to tailor target specificity through modular scFv designs.

Materials and Methods

Chimeric antigen receptor designs and constructs

The DNA fragments of different CAR genes were designed in BioEdit 7.2 and the gBlock fragments were synthesized by Integrated DNA Technologies (IDT). After ligating to 2nd

generation packaging vector, the CAR-containing vectors were used for lentivirus packaging with SFFV promoter for immortalized cell lines and GFAP promoter for primary astrocytes. The AAV-PHP.eB constructs and viruses were produced by BrainVTA (Wuhan) Co.,Ltd. based on DNA sequences provided by YC and MC.

Retroviral transfection of immortalized astrocytes

Lentiviral vectors were transfected into Lenti-X 293T cells using a second-generation lentiviral system packaging (Addgene) and viral supernatants were collected two days later. SV40T immortalized mouse astrocyte cells (in-house stock) were transduced with supernatants of transfected packaging cells with 2 μg/ml polybrene using spin infection at 1800 r.p.m. for 45 min. $EGFP^+$ cells were sorted by ARIA-II at flow cytometry core at Washington University in St. Louis. Final cell lines were frozen and stocked at −80°C until further use. Long-term storage aliquots were kept in liquid nitrogen.

Lonza primary astrocyte preparation

Cryopreserved primary mouse astrocytes (#M-AsM-330, Lonza Bioscience) were thawed and cell suspension (1×10^6 cell) was transferred into a T75 flask to initiate culture process. The initial culture was maintained in ABMTM basal medium (#CC-3187, Lonza Bioscience) at 37 °C in a humidified 5% CO_2 incubator for 6 hours to allow astrocyte recovery. After the recovery phase, astrocyte cultures were maintained in ABMTM basal medium (#CC-3187, Lonza Bioscience) supplemented with AGMTM SingleQuots (#CC-4123, Lonza Bioscience) which includes 10% fetal bovine serum (FBS), 1x L-Glutamine, 1x GA-1000, 1x ascorbic acid, 1x HEGF, and 1x insulin. Cultures were maintained at 37 °C in a humidified 5% CO_2 incubator for 7–10 days to allow astrocyte differentiation with a fresh medium change every 4 days. After 95% confluent monolayer forms, astrocytes were then trypsinized, harvested, and re-plated into 24-well plates (50,000 cells/well) for lentiviral transduction for 5 days. Following transduction, lentiviral-containing medium was replaced with ABMTM basal medium (#CC-3187, Lonza Bioscience) supplemented with AGMTM SingleQuots (#CC-4123, Lonza Bioscience) for an additional 2 days to restore astrocytic homeostasis before phagocytosis and degradation experiments.

Primary mixed glial culture preparation

Cortical tissues were dissected individually from P3–P5 C57BL/6 pups, carefully freed of meninges, and dissociated in ice-cold HBSS using trypsin and DNase to obtain a single-cell suspension. Cells from each pup were plated separately on Gibco™ Geltrex (#A1413302, ThermoFisher)-coated 6-well plates and in one T75 flask per pup to generate biological replicates. Cultures were maintained in high-glucose Dulbecco's Modified Eagle Medium (DMEM) supplemented with 10% fetal bovine serum (FBS), 1% penicillin/streptomycin, 1x Glutamax, and 1x sodium pyruvate at 37 °C in a humidified 5% CO_2 incubator for 7–10 days to allow for astrocyte differentiation. To deplete microglia and precursor cells, cultures in 6-well plates were shaken for 2 hours at 120 r.p.m. and floating cells removed, leaving behind a confluent astrocyte monolayer. Cells were then trypsinized and plated into pre-coated 48-well plates (10,000 cells/well) for CAR-AAV infection (2×10^6 vg/cell) for

72 h. Following infection, the AAV-containing medium was replaced with standard culture medium for an additional 3 days to restore astrocytic homeostasis. In parallel, cultures in T75 flasks were shaken to harvest microglia, which were subsequently transferred into CAR-expressing astrocyte cultures (20,000 microglia/well) to complete the mixed glial culture (Fig. S2A).

Aβ42 labeling and oligomers/fibrils preparation

Human Aβ42 peptide was purchased from GenScript (#RP10017). Monomeric Aβ42 was prepared in dimethyl sulfoxide following previous literature and conjugated with AlexaFluor-594, −647 or pHrodo Red NHS Ester (#A20004, A20006 and P36011, Invitrogen), molar ratio protein:dye = 1:5 in sodium bicarbonate buffer (pH 8.5) at room temperature overnight. Unconjugated dye was removed after 24-h 3.5-kDa cutoff dialysis in H_2O at 4°C. Then, Aβ42–594/647/pHrodo peptide was dried with speed vacuum at room temperature overnight. Aβ42–594/647/pHrodo oligomers were prepared following the same protocol (88) and dialyzed to phosphate-buffered saline (PBS) for 3 days. Final products were prepared into 10 μM aliquots and stored at −80°C until further use.

AD-tau, hTau fibrils, α-Synuclein PFF and myelin labeling and stock preparation

AD-tau was from the in-house stock in Holtzman lab. Human recombinant Tau-441 (2N4R) P301S mutant protein pre-formed fibrils were purchased from StressMarq Bioscience Inc. (SPR-329). The α-Synuclein PFF was from the in-house stock from Albert A. Davis lab at WashU. The myelin debris was collected from the myelin layer in the brain dissociation step by Adult Brain Dissociation Kit (#130-107-677, Miltenyi Biotec). All the materials were labeled with pHrodo Deep Red TFP Ester (succinimidyl ester) (#P35359, Invitrogen) (pHrodoAPC) in the same procedure as described. Final pHrodoAPC-labeled products were prepared into 10 μM aliquots and stored at −80°C until needed.

Phagocytosis and degradation experiments

Before the phagocytosis or degradation assay, immortalized astrocytes described above were recovered in DMEM differentiation media for 2 days. When fully recovered immortalized astrocytes were 70% confluent, non–tissue culture–treated 96-well plates were seeded with 20,000 cells per well in five replicates for each CAR construct in DMEM media for a phagocytosis/degradation assay the next day. The primary astrocytes were either differentiated and plated for 1 week (Lonza) or freshly isolated to differentiate into mixed glial culture and replated for 1 week (ex vivo mixed glial culture) to reach confluency. Then confluent primary astrocytes were spin-infected by freshly produced Crene-CAR- or Adu-CAR-expressing Lentivirus with GFAP promoter with the same approach as described earlier. For the phagocytosis assay, oAβ42-pHrodo were added into each well at 200 nM for 4h for immortalized astrocytes or 8h for primary astrocytes. For degradation assay with immortalized astrocytes, all cells were treated with oAβ42-pHrodo at 200 nM for 4h and switched to normal media for 0 and 24h before being harvested. For degradation assay with primary astrocytes, all cells were treated with fAβ42–647 at 200 nM for 8h and switched to normal media for 0 and 72h before being harvested. For surface binding assay, pre-chilled astrocytes were treated with monomeric Aβ42-AlexaFluor-647 at 100 nM for 1h at 4 °C. After washing with PBS twice, all cells were resuspended with MACS buffer (PBS, 2 mM

EDTA, and 0.5% BSA), and flow cytometry was performed on a BD FACS Calibur/BD X20/BD Canto II System at the flow cytometry core at Washington University in St. Louis. GFP (GreenLantern) signal was determined by FL1 (FITC) and Deep Red pHrodo signal was determined by FL4 Far Red (APC) and further analyzed by FlowJo.

Animals

The 5XFAD mice were purchased from JAX lab, which is on a C57BL/6 background. The WT (C57BL/6) control mice were from the same breeding but without transgene in-house. All mice were bred and housed in specific pathogen-free conditions. The Institutional Animal Care and Use Committee at Washington University in St. Louis approved all protocols used in this study. Age- and sex-matched animals used for amyloid pathology tests were euthanized at 5 months of age (early treatment) and 9 months of age (late treatment), with each experimental group containing both transgenic and non-transgenic mice. The brains of transgene-positive animals were collected.

AAV-PHP.eB intravenous injection

As described in previous literature (43), one-time intravenous administration of AAV-PHP.eB-CAR vectors were injected into the retro-orbital sinus of adult 5XFAD mice (2.5 months of age for early treatment and 6 months of age for the late treatment). For the viral safety assessment, WT mice were injected at 4 months of age. The retro-orbital sinus administration of 100 μL (7×10^{12} vg/mL) virus was using 70 μL of frozen stock viruses (1×10^{13} vg/mL) from BrainVTA (Wuhan) Co.,Ltd. with 30 μL of sterile Gibco™ PBS (#10010023, ThermoFisher), mixed prior to injections.

Animal behavioral tests

General design of behavioral tests: AAV-infected 5xFAD and WT mice were evaluated for differences in behavior. Following habituation and handling in the Washington University Animal Behavior Core, mice were assessed for Locomotor Activity, Spontaneous Alternation Y maze, Elevated Plus Maze, and Fear Conditioning. All tests were conducted during the light phase of the light/dark cycle, by a female experimenter blind to the genotype of the mice.

One-hour locomotor activity and open-field behavior test: Motor and exploratory behavior of mice were evaluated over a 1-h period in transparent (47.6 × 25.4 × 20.6 cm high) polystyrene enclosures. Each cage was surrounded by a frame containing a 4 × 8 matrix of photocell pairs, the output of which was fed to an on-line computer (Hamilton-Kinder, LLC, Poway, CA). The system software (Hamilton-Kinder, LLC) was used to define a 33 × 11 cm central zone and a peripheral or surrounding zone that was 5.5 cm wide with the sides of the cage being the outermost boundary. This peripheral area extended along the entire perimeter of the cage. Variables that were analyzed included the total number of ambulations and rearing on hindlimbs, as well as the number of entries, the time spent, and the distance traveled in the center area as well as the distance traveled in the periphery surrounding the center.

Spontaneous alternation Y-maze: Testing was conducted according to our previously published procedures. Briefly, this involved placing a mouse in one arm of a Y-maze that contained three arms that were 10.5 cm wide, 40 cm long and 20.5 cm deep where an arm was oriented at 120° with respect to each successive other arm. Mice were allowed to explore the maze for 8 min and entry into an arm was scored only when the hindlimbs had completely entered the arm. An alternation was defined as any three consecutive choices of three different arms without re-exploration of a previously visited arm. Dependent variables included the number of alternations and arm entries along with the percentage of alternations, which was determined by dividing the total number of alternations by the total number of entries minus 2, then multiplying by 100.

Elevated plus maze (EPM) test: EPM was conducted to evaluate anxiety in mice as previously described (63). Briefly, a 5 minute trial was conducted in a dimly lit room using a standard mouse EPM provided by Kinder Scientific. The EPM consists of a 5×5 cm black acrylic surface positioned 63 cm above the floor equipped with photo beam pairs to monitor the movement of the mice. Four arms extend from a central area. Each arm measures 35 cm in length and 5 cm in width (two open and two with 15 cm height wells). Mice were placed in the center square that connects the open and closed arms and allowed to explore during the 5-min trial. The MotorMonitor software measures various parameters such as duration, distance traveled, entries, and time at rest in each zone (closed arms, open arms, and center area) by quantifying beam breaks.

Conditioned fear: A conditioning protocol similar to previously described was used to train and test mice using two clear-plastic conditioning chambers (26 × 18 × 18 cm high) (Med-Associates, St. Albans, VT) which were easily distinguished by different olfactory, visual, and tactile cues present in each chamber (Chamber 1 – metal grid floor, metal walls, mint scent; Chamber 2 – solid acrylic floor, black acrylic walls, coconut scent). On the first day, each mouse was placed into the conditioning chamber (Chamber 1) for 5 min and freezing behavior was quantified during a 2 min baseline period. Freezing (no movement except that associated with respiration) was quantified using FreezeFrame image analysis software (Actimetrics, Evanston, IL) which allows for simultaneous visualization of behavior while adjusting for a “freezing threshold” during 0.75 s intervals. After baseline measurements, a conditioned stimulus (CS) consisting of an 80 dB tone (white noise) was presented for 20 s followed by an unconditioned stimulus (US) consisting of a 1 s, 1.0 mA continuous foot shock. This tone-shock (T/S) pairing was repeated each minute over the next 2 min, and freezing was quantified after each of the three tone-shock pairings. Twenty-four hours after training, each mouse was placed back into the original conditioning chamber (Chamber 1) to test for fear conditioning to the contextual cues in the chamber. This involved quantifying freezing over an 8 min period without the tone or shock being present. Forty-eight hours after the contextual test, the mice were evaluated on the auditory cue component of the conditioned fear procedure, which included placing each mouse into the other chamber (Chamber 2) containing distinctly different cues. Freezing was quantified during a 2 min “altered context” baseline period as well as over a subsequent 8 min period during which the auditory cue (CS) was presented.

Brain isolation and fixation

Whole brain samples for AAV-CAR injected cohorts were collected after perfusion. The brains were dissected and cut into two hemispheres: the right hemisphere was fixed in 4% paraformaldehyde for at least 48 h and the left hemisphere was further micro dissected into anterior cortex, posterior cortex, and hippocampus, followed by flash-freezing in 2-methylbutane on dry ice and subsequently stored at −80 °C until needed. The right brain hemispheres were cut coronally into 30-μm sections on a freezing sliding microtome (SM1020R, Leica) and stored in cryoprotectant solution (0.2 M PBS, 15% sucrose, 33% ethylene glycol) at −20°C until use. For samples from the *in vivo* phagocytosis experiment, the injected hippocampus was dissected from the whole brain samples for AAV-CAR injected cohorts collected after perfusion and kept in DPBS buffer with calcium and magnesium (#14040117, ThermoFisher) for glial cell isolation and flow cytometry.

Stereotactic intracerebral injections of AlexaFluor-647-labeled Aβ42 fibrils

After AAV-infection for 4 weeks, WT mice were anaesthetized with isoflurane and immobilized in a stereotaxic frame (Kopf Instruments). A 0.5- to 1.0-cm-long incision was made in the shaved and sterilized skin to expose the bregma. Before intracerebral injection, Aβ42–647 fibril aliquots were thawed on ice and sonicated with 50% amplitude for 30s. 1μg Aβ42–647 fibrils were injected into the dentate gyrus at specific stereotaxic coordinates (anterior/posterior, −2.5 mm; medial/lateral, −2.0 mm; dorsal/ventral, −2.2 mm) using a Hamilton syringe (#80265–1702RNR, #7803–07, Hamilton). The needle was retained for an additional 5 min before it was slowly withdrawn. The incision was cleaned with povidone-iodine antiseptic solution and sutured. Mice were allowed to recover on a 37°C heating pad and monitored for any signs of stress. Food and water were provided ad libitum. Three days after the injection, mice were euthanized, and brains were harvested for glial cell extraction and flow cytometry.

Brain dissociation and flow cytometry for in vivo phagocytosis

Mice were perfused with pre-chilled DPBS containing 0.3% heparin to remove blood contamination. Hippocampi tissues were extracted followed by microdissection of the hippocampi that had been injected with AlexaFluor-647-labeled Aβ42 fibrils, where the contralateral hippocampi were collected as internal negative controls for flow cytometry gating. Single-cell suspensions from the hippocampi were prepared using the Adult Brain Dissociation Kit (#130-107-677, Miltenyi Biotec) following the manufacturer’s instructions.

All subsequent steps for flow cytometry were performed in MACS buffer on ice or using a 4 °C centrifuge. Cell suspensions were first incubated with anti-CD16/32 Fc block (#C247, Leinco Tech) for 5 minutes, then stained for 20 minutes with CD45-BV510, CD11b-APC/Cy7 (#103137, #101225, Biolegend), and ACSA2-PE (#130-123-284, Miltenyi Biotec). After washing, cells were analyzed on Cytek Aurora with DAPI used as a live/dead marker. GFP was intrinsically expressed by astrocytes transduced with the CAR-AAV constructs, and cells containing Aβ42 fibrils were identified by AlexaFluor-647 labeling on the fibrils. Flow cytometric data were analyzed using FlowJo, and statistical analyses were performed with Prism.

Immunofluorescence staining

Floating mouse coronal brain sections with a thickness of 30μm were prepared and stained with Aβ plaque marker X34 (1:1000, #SML1954, Millipore Sigma) for 20min. Then the slices were washed by PBS and subsequently blocked using a solution containing 3% Donkey serum, 3% BSA and 0.25% Triton X-100 in PBS. Following the blocking step, the brain sections were stained with anti-IBA1 (1:500, #17198, Cell Signaling Technology), anti-GFAP (1:500, #PA1–10004, Invitrogen), anti-Olig2 (1:500, #AF2418, R&D Systems) anti-MHC-II (1:500, #107618, BioLegend; 1:250, #H1721, Leinco Tech), anti-mouse ApoE (10μg/ml, clone: HJ6.3, biotinylated, gift from Dr. Holtzman lab), anti-CD68 (1:500, #137002, BioLegend), anti-Synapsin-1/2 (1:500, #106004, Synaptic systems), anti-PSD95 (1:200, #51–6900, Thermo Fisher Scientific), anti-GPNMB (1:500, #AF2330, R&D Systems), anti-LRP1 (1:500; L2295, Sigma), anti-CSF1R (1:500; #EPR23529–26, abcam) and anti-LAMP1 (1:500; #AF4320, R&D Systems) overnight at 4 °C, followed by staining with according fluorescent secondary antibodies (1:1000, Thermo Fisher Scientific) for 2 h at room temperature. The staining of panAβ/IBA1/Clec7a was performed at room temperature for 48h for the primary staining with CLEC7A (1:50; #mabg-mdect, InvivoGen,), anti-mouse Aβ (1:500, clone: HJ3.4, biotinylated, gift from Dr. Holtzman lab), anti-IBA1 (1:500, #17198, Cell Signaling Technology). All antibodies were used in blocking buffer, and between all incubations, sections were washed for 10 min in PBS 3 times. Images were collected and analyzed as described above. Three-dimensional reconstruction and extraction of parameters were performed in Imaris (version 10.0.0), and further processing was performed using automated scripts in Matlab.

Confocal image acquisition and analysis

Images were obtained with 8 replicates from two slices per brain region per mouse for IF. Four z-stacks (20 μm) of each brain region (e.g., four from ipsilateral CTX and four from contralateral CTX) per slice were acquired on a Leica STELLARIS 5 confocal microscope and the Leica Application Suite X software (4.2.1.23810) with a 20x objective and 1,024 × 1,024 resolution. Laser and detector settings were set for the acquisition of each immunostaining combination consistently. High-resolution representative images were maximum projection from stacks imaged by confocal microscopy were 3D-reconstructed using the Leica Application Suite X software. Quantification of confocal images for LAMP1, Synapsin, PSD95, IBA1, GFAP, CD68, MHC-II and APOE around $X34^+$ plaques was performed on a semiautomated platform using MATLAB and Imaris 10 software (Bitplane) to create surfaces of each stain based on a threshold applied to all images, dilate X34 surfaces 15 μm, and colocalize various immunostained surfaces and dilated X34 surfaces. For percent voxel quantifications, colocalized volumes for each immunostained surface were summed per image and divided by the $X34^+$ extended surface. Quantification of confocal images for CD68, APOE, GPNMB, and CLEC7A in $Iba1^+$ microglia or LAMP1 and LRP1 in $GFAP^+$ astrocytes was performed by creating a surface of CD68/APOE/GPNMB/CLEC7A colocalized with Iba1 or LAMP1/LRP1 colocalized with GFAP voxels and dividing it with total IBA1 or GFAP surfaces. The final individual value was averaged from a total of 8 images per brain region per mouse. All staining experiments were imaged and quantified by a blinded investigator or labeling strategy.

Soluble and insoluble Aβ40 and Aβ42 extractions

The hippocampus samples were weighed, and then PBS buffer containing complete protease inhibitor (#11697498001, Roche) and phosSTOP phosphatase inhibitor (#04906845001, Roche) at a ratio of 20μl per milligram of tissue was added. The samples were homogenized and centrifuged at 20,627g for 30 min at 4°C, resulting in the collection of the supernatant as the PBS-soluble fraction. The pellet was then resuspended in the same volume of 5M Guanidine buffer containing complete protease inhibitor and phosSTOP phosphatase inhibitor, followed by further homogenization. The samples were incubated on a rotator for 1 hour at room temperature. Subsequently, the samples were centrifuged again, and the supernatant was collected as the PBS-insoluble guanidine fraction (Guanidine fraction). The concentrations of Aβ40 and Aβ42 were measured by ELISA.

Aβ40/42 ELISA assays

10 μg/ml of anti-Aβ40 (HJ2, generated in house) or anti-Aβ42 (HJ7.4, generated in house) were separately coated on the high-binding ELISA plates in sodium carbonate coating buffer at 4 °C overnight. After blocking with 2% BSA PBS-Tween 20 (0.05%) at 37°C for 1h, 50 μl of each sample diluted in Aβ sample buffer (0.05% PBST with 0.5% BSA and 1X complete/phosSTOP) were loaded into each well and incubated at 4 °C overnight. On the last day, 50 μl of 150 ng/ml probing antibody (HJ5.1-biotinated) were added into each well and the plates were incubated at 37 °C for 90min. Then 50 μl of streptavidin-poly-horseradish peroxidase-40 for 90 min at RT. Plates were then washed and developed with Super Slow ELISA 3,3′,5,5′-Tetramethylbenzidine (Sigma) and read at 650 nm. Between incubation steps, all plates were washed 3 times with 0.05% PBST.

Single nucleus RNA-seq

Library preparation, sequencing, and alignment

a. snRNA-seq of 5-month-old and 9-month-old mouse cortex: Nuclei were isolated from five randomly selected flash frozen mouse brain tissues per group (N = 30 mice total) and sorted for DAPI+ NeuN- nuclei by FACS. Nuclei were pooled by group, and libraries were prepared using the 10X Chromium Single-cell 3’ v3 (5-month-old) or v4 (9-month-old) kit. Sequencing was performed using an Illumina NovaSeq sequencer. Sequencing reads were analyzed with mouse reference genome GRCm39–2024-A with the addition of the WPRE and GFP transgenes. Raw sequencing data was aligned using CellRanger (5-month-old: v7.2.0; 9-month-old: v.8.0.0).

b. snRNA-seq of 5-month-old and 9-month-old mouse hippocampus: Nuclei were isolated from four randomly selected flash frozen mouse brain tissues per group and sorted for DAPI+ NeuN- Olig2- nuclei by FACS. Nuclei were pooled and libraries were prepared using the 10X Chromium Single-cell 5’ v2 kit. Sequencing was performed using an AVITI sequencer. Sequencing reads were analyzed with mouse reference GRCm39–2024-A containing the GFP transgene. Raw sequencing data was aligned using CellRanger (v9.0.0).

Quality control and preprocessing: CellRanger outputs (filtered_feature_bc_matrix) were input into Seurat(89) (v4.4.0) for analysis. Data were log-normalized, the top 2,000

variable features identified, cells clustered, and dimensionality reduction performed using UMAP. Ambient RNA was removed using SoupX autoEstCont() function. Cells were then excluded using the following criteria: < 500 or > 5000 unique genes, percent mitochondrial reads > 5%, > 25000 detected UMIs. Automated doublet removal was performed using DoubletFinder using an estimated doublet rate of 8%. Clusters consisting of doublets or cells heavily contaminated by ambient RNA that further arose during subclustering were manually removed.

Broad cluster annotation was performed using canonical markers as follows: microglia (*P2ry12, Trem2, Tmem119*), astrocytes (*Gfap, Aqp4*), oligodendrocytes (*Mbp, Olig1, Olig2, Mog*), oligodendrocyte progenitor cells (OPCs; *Pdgfra, Olig1, Olig2*), neurons (*Snap25, Rbfox3*), vascular (*Vwf, Cd34*), ependymal cells (Cilia/flagella genes such as *Cfap299, Cfap54, Dnah12*). For subclustering analyses, pseudogenes, non-coding RNAs, and unannotated genes were removed from the count matrix, and SCTransform(90) normalization was performed with nUMI and % mitochondrial reads as regressed variables. Microglia, astrocytes, and OPCs were subclustered from hippocampus Olig2- NeuN- snRNAseq data, while oligodendrocytes were subclustered from cortical NeuN- snRNAseq data (see Fig 5, S7 and S8). Differential expression testing was performed with Seurat FindMarkers() or FindAllMarkers() using the Wilcoxon ranksum test.

Astrocyte subclustering analysis: Hippocampal astrocytes were subsetted from the global Seurat object. The SCTransform() function was re-applied to recalculate Pearson residuals and variable features, as well as to re-center the scaled matrix. Annotation was performed based on diffusion map embeddings of Louvain clusters and marker genes. Transitional clusters were defined as those with intermediate gene signatures between homeostatic astrocytes and MyoC/DAA astrocytes.

Microglia subclustering analysis: Hippocampal microglia was subsetted from the global Seurat object. Data was re-normalized and variable features detected using the SCTransform() function. The 5-month-old and 9-month-old timepoints were integrated with Seurat's integration procedure using the reciprocal PCA method and 2000 integration features.

Microglia subclusters, including homeostatic microglia (HM), transitional microglia (TM), cycling microglia, interferon-responsive microglia (IFN), and MHC-II^{hi} microglia (MHC) were annotated based on markers as previously described (91,92). We noted three separate clusters that express varying levels of DAM markers, which we termed DAM-like 1/2/3. Cluster-specific expression of DAM genes can be found in Figure 6.

To include Clec7a in the count matrix, we realigned the sequencing data to a GRCm39-based reference with the Clec7a coding sequence added as previously described (92). Only the microglia barcodes were retained, and counts were normalized using SCTransform and added back to the microglia subcluster Seurat object using the CreateAssayObject() function. Transitional microglia were defined as those with intermediate gene signatures between homeostatic and disease-associated microglia.

Statistically credible changes in cell type composition: scCoda(93) was used to perform compositional analysis of astrocyte and microglia subclusters. The 5-month-old and 9-month-old timepoints were analyzed independently. Model setup was performed with group (i.e. GFP, Megf10 or Dectin1) as covariate and automatic reference cell type selection. Hamiltonian Monte Carlo sampling was performed using default parameters via the sample_hmc() function. Statistically credible changes were derived at false discovery rate (FDR) < 0.1.

Single-cell pathway analysis: Pathway analysis was performed using SCPA(94) (v1.5.4) with log-normalized counts as input in order to identify pathways with changes in multivariate distribution across comparisons. DAA and MyoC astrocytes were compared against homeostatic astrocyte clusters using the M5 gene set from MSigDB. Significantly enriched pathways retained for visualization were defined as pathways with qval > 0, adjusted p-value < 0.05, and log fold-change > 0.

Gene set enrichment analysis: Differentially expressed genes (log2FC cutoff: 0.12) were extracted, and gene set enrichment analysis was performed using a hypergeometric test with the enrichment() function from the bc3net package (v1.0.4), using the M5 gene set from the Broad Institute. Significantly enriched pathways were filtered using adjusted p-value < 0.05.

Diffusion map: Diffusion map (95) was constructed to examine the differentiation trajectories of astrocyte subclusters. The astrocyte subcluster Seurat object was converted to .h5ad format and input into Scanpy (96) (v1.1.0). The doublet clusters were removed from the astrocytes dataset. Diffusion map was constructed from PCA embeddings using 30 nearest neighbors and 15 principal components. Diffusion map coordinates were then extracted from Scanpy and added back to the Seurat object for subsequent analyses in R. Downstream tasks, including projection of external datasets and pseudotime analysis on 2D diffusion embeddings, were performed using diffusion components 2 and 3, since these best recapitulate the primary differentiation trajectories in the datasets.

Pseudotime analysis: Astrocyte subclusters were divided into either the DAA trajectory (clusters 0, 2, 3, 5) or MyoC trajectory (clusters 1, 4, 6, 7) based on the diffusion map embedding. Pseudotime analysis was performed each trajectory using slingshot(97) (v2.2.1), on diffusion components 2 and 3, with a homeostatic astrocyte subcluster as starting cluster, and either DAA or MyoC astrocytes as end cluster.

RNA velocity analysis: dropEst (v0.8.5) was used to derive the .loom file containing spliced and unspliced matrices from CellRanger-outputted BAM files. The .loom files were loaded using scvelo (98) (v0.3.3). The astrocyte subclustering dataset was also loaded, and spliced/unspliced matrices were subsetted to retain only the astrocyte barcodes. Individual samples were merged and data was filtered and normalized using default parameters. RNA velocity was estimated using the dynamical model using default parameters. RNA velocity streams were visualized using components 2 and 3 of the diffusion map.

Astrocyte-microglia ligand-receptor signaling analysis using NicheNet: Ligand-receptor signaling was performed using NicheNet(99) (v2.2.0). Log-normalized count matrices were used as input, and each of the CAR group was used as condition of interest and the GFP group as reference condition. The 5-month-old and 9-month-old time points were analyzed independently. To identify CAR-A-induced astrocytes -> microglia interactions, astrocytes were set as sender of interest and microglia were set as receivers, and the analysis was performed using the Seurat wrapper nichenet_seuratobj_aggregate(). The output data frame was filtered and prioritized based on expression of the ligand and receptors. The top 30 ligand-receptor pairs were selected for visualization with Circos plots.

Projection of snRNAseq datasets onto a reference embedding: The ProjecTILs(100) (v3.0.0) R package was used to project snRNA-seq data onto reference embeddings. Briefly, count matrix of datasets was loaded, and data were processed with lognormalization, variable feature detection, scaling, PCA, and the cluster of interest was subsetted to generate the query object. For projection of our DAA and MyoC astrocyte clusters, the reference object was generated from a Seurat object containing diffusion map embeddings from Habib et al. For projection of DAM1 and DAM2 clusters from Keren-Shaul et al., the reference was generated from our microglia Seurat object.

Module scores to identify cell types underlying differentially expressed genes: To determine subclusters responsible for up- and down-regulated genes in astrocytes and microglia, cells were scored based on their aggregate expression of the up- or down-regulated genes. This was performed using the AddModuleScore_UCell() function in the UCell(101) (v1.3.1) R package. The average upregulated/downregulated genes module score for each cluster was used to rank the clusters for their contribution to differentially expressed genes.

Data analysis and statistics

GraphPad Prism 9.0 was used to perform all statistical analyses. Data are presented as means ± SEM. Data were checked for normality using the Shapiro-Wilk method, D'Agostino and Pearson normality test, and Kolmogorov-Smirnov normality test. The statistical outliers were excluded by the ROUT method (Q = 1%) in GraphPad Prism. Statistical significance between groups with normally distributed data was calculated by two-way ANOVA with Holm-Šidák correction for multiple comparison or one-way ANOVA with Tukey correction for group-wise comparisons, unless otherwise noted in the figure legends. * ($p < 0.05$), ** ($p < 0.01$), *** ($p < 0.001$), **** ($p < 0.0001$) or ns (not significant).

Supplementary Material

Refer to Web version on PubMed Central for supplementary material.

Acknowledgments:

We thank the Washington University Center for Cellular Imaging for assistance in imaging studies, and the Flow Cytometry Core at Washington University for sorting. Graphical schematics were created with BioRender.com. We thank Samira Parhizkar and Fareeha Saadi for their kind sharing of instrument time. We thank Albeit A. Davis for

his gift of α-Synuclein PFF stock. We thank Gary Grajales-Reyes for early input and discussions that helped launch this project.

Funding:

This work was supported by NIH grants RF1 AG051485, R21 AG059176 and P01 AG078106 to MC; the Cure Alzheimer's Fund to MC; the Carol and Gene Ludwig Family Foundation to MC; and Fred and Ginger Haberle Charitable Fund at East Texas Communities Foundation to MC.

Competing interests:

MC and YC have a patent pending on CAR-A constructs (PCT/US25/41329). MC cofounded and is on the scientific advisory board of Halyardtx and BioClec, is a member of the scientific advisory board of Vigil; receives research support from Ono Pharmaceutical; is a consultant for CST and Pfizer. DMH cofounded and is on the scientific advisory board of C2N Diagnostics. DMH is on the scientific advisory board of Denali, Genentech, and Cajal Neuroscience, and consults for Asteroid. CY is on the scientific advisory board for Hoth Therapeutics and consultation for Varro Life Sciences.

Data and materials availability:

All data associated with this study are present in the paper or the Supplementary Materials. RNA-seq data is available on GEO (GSE309604). CAR-A constructs will be available from the corresponding authors under a material transfer agreement with Washington University in St. Louis.

References and Notes

1. 2024 Alzheimer's disease facts and figures. Alzheimers. Dement 20, 3708–3821 (2024). [PubMed: 38689398]
2. Tolar M, Abushakra S, Sabbagh M, The path forward in Alzheimer's disease therapeutics: Reevaluating the amyloid cascade hypothesis. Alzheimers. Dement 16, 1553–1560 (2020). [PubMed: 31706733]
3. Mary A, Mancuso R, Heneka MT, Immune Activation in Alzheimer Disease. Annu. Rev. Immunol 42, 585–613 (2024). [PubMed: 38424470]
4. Kurkinen M, Fułek M, Fułek K, Beszłej JA, Kurpas D, Leszek J, The Amyloid Cascade Hypothesis in Alzheimer's Disease: Should We Change Our Thinking? Biomolecules 13 (2023).
5. Frisoni GB, Altomare D, Thal DR, Ribaldi F, van der Kant R, Ossenkoppele R, Blennow K, Cummings J, van Duijn C, Nilsson PM, Dietrich P-Y, Scheltens P, Dubois B, The probabilistic model of Alzheimer disease: the amyloid hypothesis revised. Nat. Rev. Neurosci 23, 53–66 (2022). [PubMed: 34815562]
6. Martens YA, Zhao N, Liu C-C, Kanekiyo T, Yang AJ, Goate AM, Holtzman DM, Bu G, ApoE Cascade Hypothesis in the pathogenesis of Alzheimer's disease and related dementias. Neuron 110, 1304–1317 (2022). [PubMed: 35298921]
7. Murphy KM, Weaver C, Janeway's Immunobiology (Garland Science/Taylor & Francis Group, LLC, 2017; https://play.google.com/store/books/details?id=YH1djwEACAAJ).
8. Bateman RJ, Li Y, McDade EM, Llibre-Guerra JJ, Clifford DB, Atri A, Mills SL, Santacruz AM, Wang G, Supnet C, Benzinger TLS, Gordon BA, Ibanez L, Klein G, Baudler M, Doody RS, Delmar P, Kerchner GA, Bittner T, Wojtowicz J, Bonni A, Fontoura P, Hofmann C, Kulic L, Hassenstab J, Aschenbrenner AJ, Perrin RJ, Cruchaga C, Renton AE, Xiong C, Goate AA, Morris JC, Holtzman DM, Snider BJ, Mummery C, Brooks WS, Wallon D, Berman SB, Roberson E, Masters CL, Galasko DR, Jayadev S, Sanchez-Valle R, Pariente J, Kinsella J, van Dyck CH, Gauthier S, Hsiung G-YR, Masellis M, Dubois B, Honig LS, Jack CR, Daniels A, Aguillón D, Allegri R, Chhatwal J, Day G, Fox NC, Huey E, Ikeuchi T, Jucker M, Lee J-H, Levey AI, Levin J, Lopera F, Roh J, Rosa-Neto P, Schofield PR, Dominantly Inherited Alzheimer's Disease-Trials Unit, Safety and efficacy of long-term gantenerumab treatment in dominantly inherited Alzheimer's disease: an

open-label extension of the phase 2/3 multicentre, randomised, double-blind, placebo-controlled platform DIAN-TU trial. Lancet Neurol. 24, 316–330 (2025). [PubMed: 40120616]

9. Ross EL, Weinberg MS, Arnold SE, Cost-effectiveness of Aducanumab and Donanemab for Early Alzheimer Disease in the US. JAMA Neurol. 79, 478–487 (2022). [PubMed: 35344024]
10. Brockmann R, Nixon J, Love BL, Yunusa I, Impacts of FDA approval and Medicare restriction on antiamyloid therapies for Alzheimer's disease: patient outcomes, healthcare costs, and drug development. Lancet Reg Health Am 20, 100467 (2023). [PubMed: 36908502]
11. Jönsson L, Wimo A, Handels R, Johansson G, Boada M, Engelborghs S, Frölich L, Jessen F, Kehoe PG, Kramberger M, de Mendonça A, Ousset PJ, Scarmeas N, Visser PJ, Waldemar G, Winblad B, The affordability of lecanemab, an amyloid-targeting therapy for Alzheimer's disease: an EADC-EC viewpoint. Lancet Reg Health Eur 29, 100657 (2023). [PubMed: 37251789]
12. Withington CG, Turner RS, Amyloid-Related Imaging Abnormalities With Anti-amyloid Antibodies for the Treatment of Dementia Due to Alzheimer's Disease. Front. Neurol 13, 862369 (2022). [PubMed: 35401412]
13. Reish NJ, Jamshidi P, Stamm B, Flanagan ME, Sugg E, Tang M, Donohue KL, McCord M, Krumpelman C, Mesulam M-M, Castellani R, Chou SH-Y, Multiple Cerebral Hemorrhages in a Patient Receiving Lecanemab and Treated with t-PA for Stroke. N. Engl. J. Med 388, 478–479 (2023). [PubMed: 36599061]
14. Self WK, Holtzman DM, Emerging diagnostics and therapeutics for Alzheimer disease. Nat. Med 29, 2187–2199 (2023). [PubMed: 37667136]
15. McDade E, Bateman RJ, Stop Alzheimer's before it starts. Nature 547, 153–155 (2017). [PubMed: 28703214]
16. Bateman RJ, Benzinger TL, Berry S, Clifford DB, Duggan C, Fagan AM, Fanning K, Farlow MR, Hassenstab J, McDade EM, Mills S, Paumier K, Quintana M, Salloway SP, Santacruz A, Schneider LS, Wang G, Xiong C, DIAN-TU Pharma Consortium for the Dominantly Inherited Alzheimer Network, The DIAN-TU Next Generation Alzheimer's prevention trial: Adaptive design and disease progression model. Alzheimers. Dement 13, 8–19 (2017). [PubMed: 27583651]
17. Long JM, Holtzman DM, Alzheimer Disease: An Update on Pathobiology and Treatment Strategies. Cell 179, 312–339 (2019). [PubMed: 31564456]
18. Sims JR, Zimmer JA, Evans CD, Lu M, Ardayfio P, Sparks J, Wessels AM, Shcherbinin S, Wang H, Monkul Nery ES, Collins EC, Solomon P, Salloway S, Apostolova LG, Hansson O, Ritchie C, Brooks DA, Mintun M, Skovronsky DM, TRAILBLAZER-ALZ 2 Investigators, Donanemab in Early Symptomatic Alzheimer Disease: The TRAILBLAZER-ALZ 2 Randomized Clinical Trial. JAMA 330, 512–527 (2023). [PubMed: 37459141]
19. van Dyck CH, Swanson CJ, Aisen P, Bateman RJ, Chen C, Gee M, Kanekiyo M, Li D, Reyderman L, Cohen S, Froelich L, Katayama S, Sabbagh M, Vellas B, Watson D, Dhadda S, Irizarry M, Kramer LD, Iwatsubo T, Lecanemab in early Alzheimer's disease. N. Engl. J. Med 388, 9–21 (2023). [PubMed: 36449413]
20. Cadiz MP, Gibson KA, Todd KT, Nascari DG, Massa N, Lilley MT, Olney KC, Al-Amin MM, Jiang H, Holtzman DM, Fryer JD, Aducanumab anti-amyloid immunotherapy induces sustained microglial and immune alterations. J. Exp. Med 221 (2024).
21. Morrissey MA, Williamson AP, Steinbach AM, Roberts EW, Kern N, Headley MB, Vale RD, Chimeric antigen receptors that trigger phagocytosis. Elife 7 (2018).
22. Klichinsky M, Ruella M, Shestova O, Lu XM, Best A, Zeeman M, Schmierer M, Gabrusiewicz K, Anderson NR, Petty NE, Cummins KD, Shen F, Shan X, Veliz K, Blouch K, Yashiro-Ohtani Y, Kenderian SS, Kim MY, O'Connor RS, Wallace SR, Kozlowski MS, Marchione DM, Shestov M, Garcia BA, June CH, Gill S, Human chimeric antigen receptor macrophages for cancer immunotherapy. Nat. Biotechnol 38, 947–953 (2020). [PubMed: 32361713]
23. June CH, O'Connor RS, Kawalekar OU, Ghassemi S, Milone MC, CAR T cell immunotherapy for human cancer. Science 359, 1361–1365 (2018). [PubMed: 29567707]
24. Baker DJ, Arany Z, Baur JA, Epstein JA, June CH, CAR T therapy beyond cancer: the evolution of a living drug. Nature 619, 707–715 (2023). [PubMed: 37495877]

25. Zhang W, Liu L, Su H, Liu Q, Shen J, Dai H, Zheng W, Lu Y, Zhang W, Bei Y, Shen P, Chimeric antigen receptor macrophage therapy for breast tumours mediated by targeting the tumour extracellular matrix. Br. J. Cancer 121, 837–845 (2019). [PubMed: 31570753]
26. Gatto L, Nunno VD, Franceschi E, Brandes AA, Chimeric antigen receptor macrophage for glioblastoma immunotherapy: the way forward. Immunotherapy 13, 879–883 (2021). [PubMed: 34078139]
27. Kim AB, Xiao Q, Yan P, Pan Q, Pandey G, Grathwohl S, Gonzales E, Xu I, Cho Y, Haecker H, Epelman S, Diwan A, Lee J-M, DeSelm CJ, Chimeric antigen receptor macrophages target and resorb amyloid plaques. JCI Insight 9 (2024).
28. Heiss CN, Riise R, Hanse E, Fruhwürth S, Zetterberg H, Björefeldt A, Expression of anti-amyloid CARs in microglia promotes efficient and selective phagocytosis of Aβ1−42. Gene Ther. 32, 333–338 (2025). [PubMed: 40210700]
29. Sailor KA, Agoranos G, López-Manzaneda S, Tada S, Gillet-Legrand B, Guerinot C, Masson J-B, Vestergaard CL, Bonner M, Gagnidze K, Veres G, Lledo P-M, Cartier N, Hematopoietic stem cell transplantation chemotherapy causes microglia senescence and peripheral macrophage engraftment in the brain. Nat. Med 28, 517–527 (2022). [PubMed: 35190726]
30. Yoo Y, Neumayer G, Shibuya Y, Mader MM-D, Wernig M, A cell therapy approach to restore microglial Trem2 function in a mouse model of Alzheimer's disease. Cell Stem Cell 30, 1043–1053.e6 (2023). [PubMed: 37541210]
31. Shibuya Y, Kumar KK, Mader MM-D, Yoo Y, Ayala LA, Zhou M, Mohr MA, Neumayer G, Kumar I, Yamamoto R, Marcoux P, Liou B, Bennett FC, Nakauchi H, Sun Y, Chen X, Heppner FL, Wyss-Coray T, Südhof TC, Wernig M, Treatment of a genetic brain disease by CNS-wide microglia replacement. Sci. Transl. Med 14, eabl9945 (2022). [PubMed: 35294256]
32. Chadarevian JP, Lombroso SI, Peet GC, Hasselmann J, Tu C, Marzan DE, Capocchi J, Purnell FS, Nemec KM, Lahian A, Escobar A, England W, Chaluvadi S, O'Brien CA, Yaqoob F, Aisenberg WH, Porras-Paniagua M, Bennett ML, Davtyan H, Spitale RC, Blurton-Jones M, Bennett FC, Engineering an inhibitor-resistant human CSF1R variant for microglia replacement. J. Exp. Med 220 (2023).
33. Elmore MRP, Hohsfield LA, Kramár EA, Soreq L, Lee RJ, Pham ST, Najafi AR, Spangenberg EE, Wood MA, West BL, Green KN, Replacement of microglia in the aged brain reverses cognitive, synaptic, and neuronal deficits in mice. Aging Cell 17, e12832 (2018). [PubMed: 30276955]
34. Lin R, Zhou Y, Yan T, Wang R, Li H, Wu Z, Zhang X, Zhou X, Zhao F, Zhang L, Li Y, Luo M, Directed evolution of adeno-associated virus for efficient gene delivery to microglia. Nat. Methods 19, 976–985 (2022). [PubMed: 35879607]
35. Okada Y, Hosoi N, Matsuzaki Y, Fukai Y, Hiraga A, Nakai J, Nitta K, Shinohara Y, Konno A, Hirai H, Development of microglia-targeting adeno-associated viral vectors as tools to study microglial behavior *in vivo*. Commun Biol 5, 1224 (2022). [PubMed: 36369525]
36. Maes ME, Colombo G, Schulz R, Siegert S, Targeting microglia with lentivirus and AAV: Recent advances and remaining challenges. Neurosci. Lett 707, 134310 (2019). [PubMed: 31158432]
37. Liddelow SA, Barres BA, Reactive Astrocytes: Production, Function, and Therapeutic Potential. Immunity 46, 957–967 (2017). [PubMed: 28636962]
38. Patani R, Hardingham GE, Liddelow SA, Functional roles of reactive astrocytes in neuroinflammation and neurodegeneration. Nat. Rev. Neurol 19, 395–409 (2023). [PubMed: 37308616]
39. Endo F, Kasai A, Soto JS, Yu X, Qu Z, Hashimoto H, Gradinaru V, Kawaguchi R, Khakh BS, Molecular basis of astrocyte diversity and morphology across the CNS in health and disease. Science 378, eadc9020 (2022). [PubMed: 36378959]
40. Koistinaho M, Lin S, Wu X, Esterman M, Koger D, Hanson J, Higgs R, Liu F, Malkani S, Bales KR, Paul SM, Apolipoprotein E promotes astrocyte colocalization and degradation of deposited amyloid-beta peptides. Nat. Med 10, 719–726 (2004). [PubMed: 15195085]
41. Wyss-Coray T, Loike JD, Brionne TC, Lu E, Anankov R, Yan F, Silverstein SC, Husemann J, Adult mouse astrocytes degrade amyloid-beta *in vitro* and in situ. Nat. Med 9, 453–457 (2003). [PubMed: 12612547]

42. Konishi H, Okamoto T, Hara Y, Komine O, Tamada H, Maeda M, Osako F, Kobayashi M, Nishiyama A, Kataoka Y, Takai T, Udagawa N, Jung S, Ozato K, Tamura T, Tsuda M, Yamanaka K, Ogi T, Sato K, Kiyama H, Astrocytic phagocytosis is a compensatory mechanism for microglial dysfunction. EMBO J. 39, e104464 (2020). [PubMed: 32959911]
43. Chan KY, Jang MJ, Yoo BB, Greenbaum A, Ravi N, Wu W-L, Sánchez-Guardado L, Lois C, Mazmanian SK, Deverman BE, Gradinaru V, Engineered AAVs for efficient noninvasive gene delivery to the central and peripheral nervous systems. Nat. Neurosci 20, 1172–1179 (2017). [PubMed: 28671695]
44. Challis RC, Ravindra Kumar S, Chen X, Goertsen D, Coughlin GM, Hori AM, Chuapoco MR, Otis TS, Miles TF, Gradinaru V, Adeno-Associated Virus Toolkit to Target Diverse Brain Cells. Annu. Rev. Neurosci 45, 447–469 (2022). [PubMed: 35440143]
45. Paolicelli RC, Bolasco G, Pagani F, Maggi L, Scianni M, Panzanelli P, Giustetto M, Ferreira TA, Guiducci E, Dumas L, Ragozzino D, Gross CT, Synaptic pruning by microglia is necessary for normal brain development. Science 333, 1456–1458 (2011). [PubMed: 21778362]
46. Hong S, Dissing-Olesen L, Stevens B, New insights on the role of microglia in synaptic pruning in health and disease. Curr. Opin. Neurobiol 36, 128–134 (2016). [PubMed: 26745839]
47. Bosworth AP, Allen NJ, The diverse actions of astrocytes during synaptic development. Curr. Opin. Neurobiol 47, 38–43 (2017). [PubMed: 28938161]
48. Park J, Chung W-S, Astrocyte-dependent circuit remodeling by synapse phagocytosis. Curr. Opin. Neurobiol 81, 102732 (2023). [PubMed: 37247606]
49. Li Q, Barres BA, Microglia and macrophages in brain homeostasis and disease. Nat. Rev. Immunol 18, 225–242 (2018). [PubMed: 29151590]
50. Chung W-S, Clarke LE, Wang GX, Stafford BK, Sher A, Chakraborty C, Joung J, Foo LC, Thompson A, Chen C, Smith SJ, Barres BA, Astrocytes mediate synapse elimination through MEGF10 and MERTK pathways. Nature 504, 394–400 (2013). [PubMed: 24270812]
51. Li Q, Cheng Z, Zhou L, Darmanis S, Neff NF, Okamoto J, Gulati G, Bennett ML, Sun LO, Clarke LE, Marschallinger J, Yu G, Quake SR, Wyss-Coray T, Barres BA, Developmental Heterogeneity of Microglia and Brain Myeloid Cells Revealed by Deep Single-Cell RNA Sequencing. Neuron 101, 207–223.e10 (2019). [PubMed: 30606613]
52. Huang Y, Happonen KE, Burrola PG, O'Connor C, Hah N, Huang L, Nimmerjahn A, Lemke G, Microglia use TAM receptors to detect and engulf amyloid β plaques. Nat. Immunol 22, 586–594 (2021). [PubMed: 33859405]
53. Sterner RC, Sterner RM, CAR-T cell therapy: current limitations and potential strategies. Blood Cancer J. 11, 69 (2021). [PubMed: 33824268]
54. Tone K, Stappers MHT, Willment JA, Brown GD, C-type lectin receptors of the Dectin-1 cluster: Physiological roles and involvement in disease. Eur. J. Immunol 49, 2127–2133 (2019). [PubMed: 31580478]
55. Ultsch M, Li B, Maurer T, Mathieu M, Adolfsson O, Muhs A, Pfeifer A, Pihlgren M, Bainbridge TW, Reichelt M, Ernst JA, Eigenbrot C, Fuh G, Atwal JK, Watts RJ, Wang W, Structure of Crenezumab Complex with Aβ Shows Loss of β-Hairpin. Sci. Rep 6, 39374 (2016). [PubMed: 27996029]
56. van Dyck CH, Anti-Amyloid-β Monoclonal Antibodies for Alzheimer's Disease: Pitfalls and Promise. Biol. Psychiatry 83, 311–319 (2018). [PubMed: 28967385]
57. Adolfsson O, Pihlgren M, Toni N, Varisco Y, Buccarello AL, Antoniello K, Lohmann S, Piorkowska K, Gafner V, Atwal JK, Maloney J, Chen M, Gogineni A, Weimer RM, Mortensen DL, Friesenhahn M, Ho C, Paul R, Pfeifer A, Muhs A, Watts RJ, An effector-reduced anti-β-amyloid (Aβ) antibody with unique aβ binding properties promotes neuroprotection and glial engulfment of Aβ. J. Neurosci 32, 9677–9689 (2012). [PubMed: 22787053]
58. Selkoe DJ, Alzheimer disease and aducanumab: adjusting our approach. Nat. Rev. Neurol 15, 365–366 (2019). [PubMed: 31138932]
59. Arndt JW, Qian F, Smith BA, Quan C, Kilambi KP, Bush MW, Walz T, Pepinsky RB, Bussière T, Hamann S, Cameron TO, Weinreb PH, Structural and kinetic basis for the selectivity of aducanumab for aggregated forms of amyloid-β. Sci. Rep 8, 6412 (2018). [PubMed: 29686315]

60. Goertsen D, Flytzanis NC, Goeden N, Chuapoco MR, Cummins A, Chen Y, Fan Y, Zhang Q, Sharma J, Duan Y, Wang L, Feng G, Chen Y, Ip NY, Pickel J, Gradinaru V, AAV capsid variants with brain-wide transgene expression and decreased liver targeting after intravenous delivery in mouse and marmoset. Nat. Neurosci 25, 106–115 (2022). [PubMed: 34887588]

61. Ellmeier W, Sawada S, Littman DR, The regulation of CD4 and CD8 coreceptor gene expression during T cell development. Annu. Rev. Immunol 17, 523–554 (1999). [PubMed: 10358767]

62. Griffin JM, Fackelmeier B, Fong DM, Mouravlev A, Young D, O'Carroll SJ, Astrocyte-selective AAV gene therapy through the endogenous GFAP promoter results in robust transduction in the rat spinal cord following injury. Gene Ther. 26, 198–210 (2019). [PubMed: 30962538]

63. Forner S, Kawauchi S, Balderrama-Gutierrez G, Kramár EA, Matheos DP, Phan J, Javonillo DI, Tran KM, Hingco E, da Cunha C, Rezaie N, Alcantara JA, Baglietto-Vargas D, Jansen C, Neumann J, Wood MA, MacGregor GR, Mortazavi A, Tenner AJ, LaFerla FM, Green KN, Systematic phenotyping and characterization of the 5xFAD mouse model of Alzheimer's disease. Sci. Data 8, 270 (2021). [PubMed: 34654824]

64. Sasmita AO, Ong EC, Nazarenko T, Mao S, Komarek L, Thalmann M, Hantakova V, Spieth L, Berghoff SA, Barr HJ, Hingerl M, Börensen F, Hirrlinger J, Simons M, Stevens B, Depp C, Nave K-A, Parental origin of transgene modulates amyloid-β plaque burden in the 5xFAD mouse model of Alzheimer's disease. Neuron 113, 838–846.e4 (2025). [PubMed: 39837326]

65. Richard BC, Kurdakova A, Baches S, Bayer TA, Weggen S, Wirths O, Gene dosage dependent aggravation of the neurological phenotype in the 5XFAD mouse model of Alzheimer's disease. J. Alzheimers. Dis 45, 1223–1236 (2015). [PubMed: 25697701]

66. Jankowsky JL, Zheng H, Practical considerations for choosing a mouse model of Alzheimer's disease. Mol. Neurodegener 12, 89 (2017). [PubMed: 29273078]

67. Carneiro AD, Schaffer DV, Engineering novel adeno-associated viruses (AAVs) for improved delivery in the nervous system. Curr. Opin. Chem. Biol 83, 102532 (2024). [PubMed: 39342684]

68. Wang Y, Ulland TK, Ulrich JD, Song W, Tzaferis JA, Hole JT, Yuan P, Mahan TE, Shi Y, Gilfillan S, Cella M, Grutzendler J, DeMattos RB, Cirrito JR, Holtzman DM, Colonna M, TREM2-mediated early microglial response limits diffusion and toxicity of amyloid plaques. J. Exp. Med 213, 667–675 (2016). [PubMed: 27091843]

69. Chen Y, Song S, Parhizkar S, Lord J, Zhu Y, Strickland MR, Wang C, Park J, Tabor GT, Jiang H, Li K, Davis AA, Yuede CM, Colonna M, Ulrich JD, Holtzman DM, APOE3ch alters microglial response and suppresses Aβ-induced tau seeding and spread. Cell 187, 428–445.e20 (2024). [PubMed: 38086389]

70. Wang S, Sudan R, Peng V, Zhou Y, Du S, Yuede CM, Lei T, Hou J, Cai Z, Cella M, Nguyen K, Poliani PL, Beatty WL, Chen Y, Cao S, Lin K, Rodrigues C, Ellebedy AH, Gilfillan S, Brown GD, Holtzman DM, Brioschi S, Colonna M, TREM2 drives microglia response to amyloid-β via SYK-dependent and -independent pathways. Cell 185, 4153–4169.e19 (2022). [PubMed: 36306735]

71. Serrano-Pozo A, Muzikansky A, Gómez-Isla T, Growdon JH, Betensky RA, Frosch MP, Hyman BT, Differential relationships of reactive astrocytes and microglia to fibrillar amyloid deposits in Alzheimer disease. J. Neuropathol. Exp. Neurol 72, 462–471 (2013). [PubMed: 23656989]

72. Serrano-Pozo A, Mielke ML, Gómez-Isla T, Betensky RA, Growdon JH, Frosch MP, Hyman BT, Reactive glia not only associates with plaques but also parallels tangles in Alzheimer's disease. Am. J. Pathol 179, 1373–1384 (2011). [PubMed: 21777559]

73. Habib N, McCabe C, Medina S, Varshavsky M, Kitsberg D, Dvir-Szternfeld R, Green G, Dionne D, Nguyen L, Marshall JL, Chen F, Zhang F, Kaplan T, Regev A, Schwartz M, Disease-associated astrocytes in Alzheimer's disease and aging. Nat. Neurosci 23, 701–706 (2020). [PubMed: 32341542]

74. Chen Y, Colonna M, Microglia in Alzheimer's disease at single-cell level. Are there common patterns in humans and mice? J. Exp. Med 218 (2021).

75. Paolicelli RC, Sierra A, Stevens B, Tremblay M-E, Aguzzi A, Ajami B, Amit I, Audinat E, Bechmann I, Bennett M, Bennett F, Bessis A, Biber K, Bilbo S, Blurton-Jones M, Boddeke E, Brites D, Brône B, Brown GC, Butovsky O, Carson MJ, Castellano B, Colonna M, Cowley SA, Cunningham C, Davalos D, De Jager PL, de Strooper B, Denes A, Eggen BJL, Eyo U, Galea E, Garel S, Ginhoux F, Glass CK, Gokce O, Gomez-Nicola D, González B, Gordon S, Graeber MB, Greenhalgh AD, Gressens P, Greter M, Gutmann DH, Haass C, Heneka MT, Heppner FL, Hong

S, Hume DA, Jung S, Kettenmann H, Kipnis J, Koyama R, Lemke G, Lynch M, Majewska A, Malcangio M, Malm T, Mancuso R, Masuda T, Matteoli M, McColl BW, Miron VE, Molofsky AV, Monje M, Mracsko E, Nadjar A, Neher JJ, Neniskyte U, Neumann H, Noda M, Peng B, Peri F, Perry VH, Popovich PG, Pridans C, Priller J, Prinz M, Ragozzino D, Ransohoff RM, Salter MW, Schaefer A, Schafer DP, Schwartz M, Simons M, Smith CJ, Streit WJ, Tay TL, Tsai L-H, Verkhratsky A, von Bernhardi R, Wake H, Wittamer V, Wolf SA, Wu L-J, Wyss-Coray T, Microglia states and nomenclature: A field at its crossroads. Neuron 110, 3458–3483 (2022). [PubMed: 36327895]

76. Keren-Shaul H, Spinrad A, Weiner A, Matcovitch-Natan O, Dvir-Szternfeld R, Ulland TK, David E, Baruch K, Lara-Astaiso D, Toth B, Itzkovitz S, Colonna M, Schwartz M, Amit I, A Unique Microglia Type Associated with Restricting Development of Alzheimer's Disease. Cell 169, 1276–1290.e17 (2017). [PubMed: 28602351]
77. Chung W-S, Allen NJ, Eroglu C, Astrocytes Control Synapse Formation, Function, and Elimination. Cold Spring Harb. Perspect. Biol 7, a020370 (2015). [PubMed: 25663667]
78. Xu Z, Rao Y, Huang Y, Zhou T, Feng R, Xiong S, Yuan T-F, Qin S, Lu Y, Zhou X, Li X, Qin B, Mao Y, Peng B, Efficient Strategies for Microglia Replacement in the Central Nervous System. Cell Rep. 33, 108443 (2020). [PubMed: 33238120]
79. Chatterjee D, Marmion DJ, McBride JL, Manfredsson FP, Butler D, Messer A, Kordower JH, Enhanced CNS transduction from AAV.PHP.eB infusion into the cisterna magna of older adult rats compared to AAV9. Gene Ther. 29, 390–397 (2022). [PubMed: 33753910]
80. Ling Q, Herstine JA, Bradbury A, Gray SJ, AAV-based *in vivo* gene therapy for neurological disorders. Nat. Rev. Drug Discov 22, 789–806 (2023). [PubMed: 37658167]
81. Venditti CP, Safety questions for AAV gene therapy. Nat. Biotechnol 39, 24–26 (2021). [PubMed: 33199877]
82. Flotte TR, Cataltepe O, Puri A, Batista AR, Moser R, McKenna-Yasek D, Douthwright C, Gernoux G, Blackwood M, Mueller C, Tai PWL, Jiang X, Bateman S, Spanakis SG, Parzych J, Keeler AM, Abayazeed A, Rohatgi S, Gibson L, Finberg R, Barton BA, Vardar Z, Shazeeb MS, Gounis M, Tifft CJ, Eichler FS, Brown RH Jr, Martin DR, Gray-Edwards HL, Sena-Esteves M, AAV gene therapy for Tay-Sachs disease. Nat. Med 28, 251–259 (2022). [PubMed: 35145305]
83. Liu C-C, Hu J, Zhao N, Wang J, Wang N, Cirrito JR, Kanekiyo T, Holtzman DM, Bu G, Astrocytic LRP1 Mediates Brain Aβ Clearance and Impacts Amyloid Deposition. J. Neurosci 37, 4023–4031 (2017). [PubMed: 28275161]
84. Sofroniew MV, Astrocyte reactivity: Subtypes, states, and functions in CNS innate immunity. Trends Immunol. 41, 758–770 (2020). [PubMed: 32819810]
85. Lehrman EK, Wilton DK, Litvina EY, Welsh CA, Chang ST, Frouin A, Walker AJ, Heller MD, Umemori H, Chen C, Stevens B, CD47 protects synapses from excess microglia-mediated pruning during development. Neuron 100, 120–134.e6 (2018). [PubMed: 30308165]
86. Faust TE, Lee Y-H, O'Connor CD, Boyle MA, Gunner G, Durán-Laforet V, Ferrari LL, Murphy RE, Badimon A, Sakers K, Eroglu C, Ayata P, Schaefer A, Schafer DP, Microglia-astrocyte crosstalk regulates synapse remodeling via Wnt signaling. Cell 188, 5212–5230.e21 (2025). [PubMed: 40934914]
87. Minhas PS, Jones JR, Latif-Hernandez A, Sugiura Y, Durairaj AS, Wang Q, Mhatre SD, Uenaka T, Crapser J, Conley T, Ennerfelt H, Jung YJ, Liu L, Prasad P, Jenkins BC, Ay YA, Matrongolo M, Goodman R, Newmeyer T, Heard K, Kang A, Wilson EN, Yang T, Ullian EM, Serrano GE, Beach TG, Wernig M, Rabinowitz JD, Suematsu M, Longo FM, McReynolds MR, Gage FH, Andreasson KI, Restoring hippocampal glucose metabolism rescues cognition across Alzheimer's disease pathologies. Science 385, eabm6131 (2024). [PubMed: 39172838]
88. Stine WB, Jungbauer L, Yu C, LaDu MJ, Preparing synthetic Aβ in different aggregation states. Methods Mol. Biol 670, 13–32 (2011). [PubMed: 20967580]
89. Hao Y et al. , Integrated analysis of multimodal single-cell data. Cell 184, 3573–3587. e3529 (2021). [PubMed: 34062119]
90. Hafemeister C, Satija R, Normalization and variance stabilization of single-cell RNA-seq data using regularized negative binomial regression. Genome biology 20, 296 (2019). [PubMed: 31870423]

91. Chen Y, Colonna M, Microglia in Alzheimer's disease at single-cell level. Are there common patterns in humans and mice? Journal of Experimental Medicine 218, (2021).

92. Wang S et al. , TREM2 drives microglia response to amyloid-β via SYK-dependent and-independent pathways. Cell 185, 4153–4169. e4119 (2022). [PubMed: 36306735]

93. Buettner M, Ostner J, Mueller CL, Theis FJ, Schubert B, scCODA is a Bayesian model for compositional single-cell data analysis. Nature communications 12, 6876 (2021).

94. Bibby JA et al. , Systematic single-cell pathway analysis to characterize early T cell activation. Cell Reports 41, (2022).

95. Haghverdi L, Buettner F, Theis FJ, Diffusion maps for high-dimensional single-cell analysis of differentiation data. Bioinformatics 31, 2989–2998 (2015). [PubMed: 26002886]

96. Wolf FA, Angerer P, Theis FJ, SCANPY: large-scale single-cell gene expression data analysis. Genome biology 19, 1–5 (2018). [PubMed: 29301551]

97. Street K et al. , Slingshot: cell lineage and pseudotime inference for single-cell transcriptomics. BMC genomics 19, 1–16 (2018). [PubMed: 29291715]

98. Bergen V, Lange M, Peidli S, Wolf FA, Theis FJ, Generalizing RNA velocity to transient cell states through dynamical modeling. Nature biotechnology 38, 1408–1414 (2020).

99. Browaeys R, Saelens W, Saeys Y, NicheNet: modeling intercellular communication by linking ligands to target genes. Nature methods 17, 159–162 (2020). [PubMed: 31819264]

100. Andreatta M et al. , Interpretation of T cell states from single-cell transcriptomics data using reference atlases. Nature communications 12, 2965 (2021).

101. Andreatta M, Carmona SJ, UCell: Robust and scalable single-cell gene signature scoring. Computational and structural biotechnology journal 19, 3796–3798 (2021). [PubMed: 34285779]

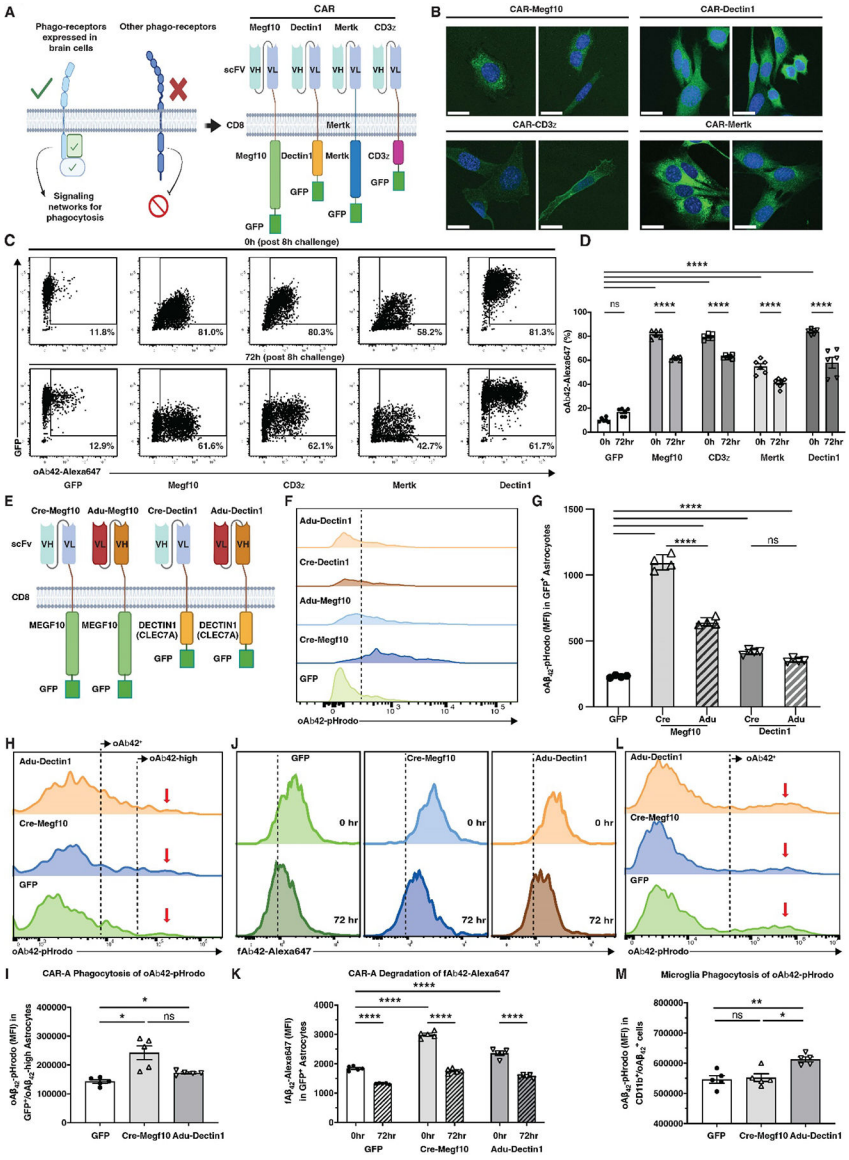

Fig. 1. *In vitro* Aβ-specific CAR designs and verifications for astrocytes.

(A) Schematic representation of the rationale used to select appropriate phagocytic receptors (left) and the designs of CARs with different intracellular signaling domains (right). (B) Confocal imaging of immortalized astrocytes transduced with the Crene-CARs, nuclei are stained with DAPI (blue). Scale bar: 20 μm. (C) Flow cytometry plots of oligomeric Aβ42–647 (oAβ42–647) uptake by Lonza primary astrocytes at 8 hours phagocytosis and 72 hours post phagocytosis. (D) Quantifications of the percentage of oAβ42–647 CAR astrocytes at 0h and 72h post 8 hours of phagocytosis. N=6. (E) Schematic representation of CAR-Megf10 and CAR-Dectin1 with different scFvs. (F) Representative flow cytometry histograms of oAβ42-pHrodo uptake by Crene-Megf10, Adu-Megf10, Crene-Dectin1 and Adu-Dectin1 astrocytes at 8 hours. (G) The mean fluorescence intensity (MFI) of oAβ42-pHrodo uptake by Crene-Megf10, Adu-Megf10, Crene-Dectin1 and Adu-Dectin1 astrocytes at 8 hours. N=4. (H) Representative flow cytometry histograms of oAβ42-pHrodo uptake

by GFP-, Crene-Megf10-, and Adu-Dectin1-expressing astrocytes in the mixed glial culture at 8 hours. Two populations of oAβ42^{+} astrocytes are indicated by labels in the panel. (I) Quantifications of the MFI of Aβ42-pHrodo uptake by GFP−, Crene-Megf10−, and Adu-Dectin1-expressing astrocytes in the mixed glial culture at 8 hours. (J) Representative flow cytometry histograms of fibrillar Aβ42–647^{+} uptake by GFP−, Crene-Megf10−, and Adu-Dectin1-expressing astrocytes at 0h and 24h post 8 hours of phagocytosis. (K) Quantifications of the MFI of fibrillar Aβ42–647^{+} uptake by GFP−, Crene-Megf10-, and Adu-Dectin1-expressing astrocytes at 0h and 24h post 8 hours of phagocytosis. (L) Representative flow cytometry histograms of oAβ42-pHrodo uptake by microglia in each mixed glial culture at 8 hours. Populations of oAβ42^{+} microglia are indicated by labels in the panel. (M) Quantifications of the MFI of Aβ42-pHrodo uptake by microglia in the mixed glial culture at 8 hours. N=5. All data presented as mean ± SEM with technical replicates except that Fig. 1I, K, M with biological replicates.

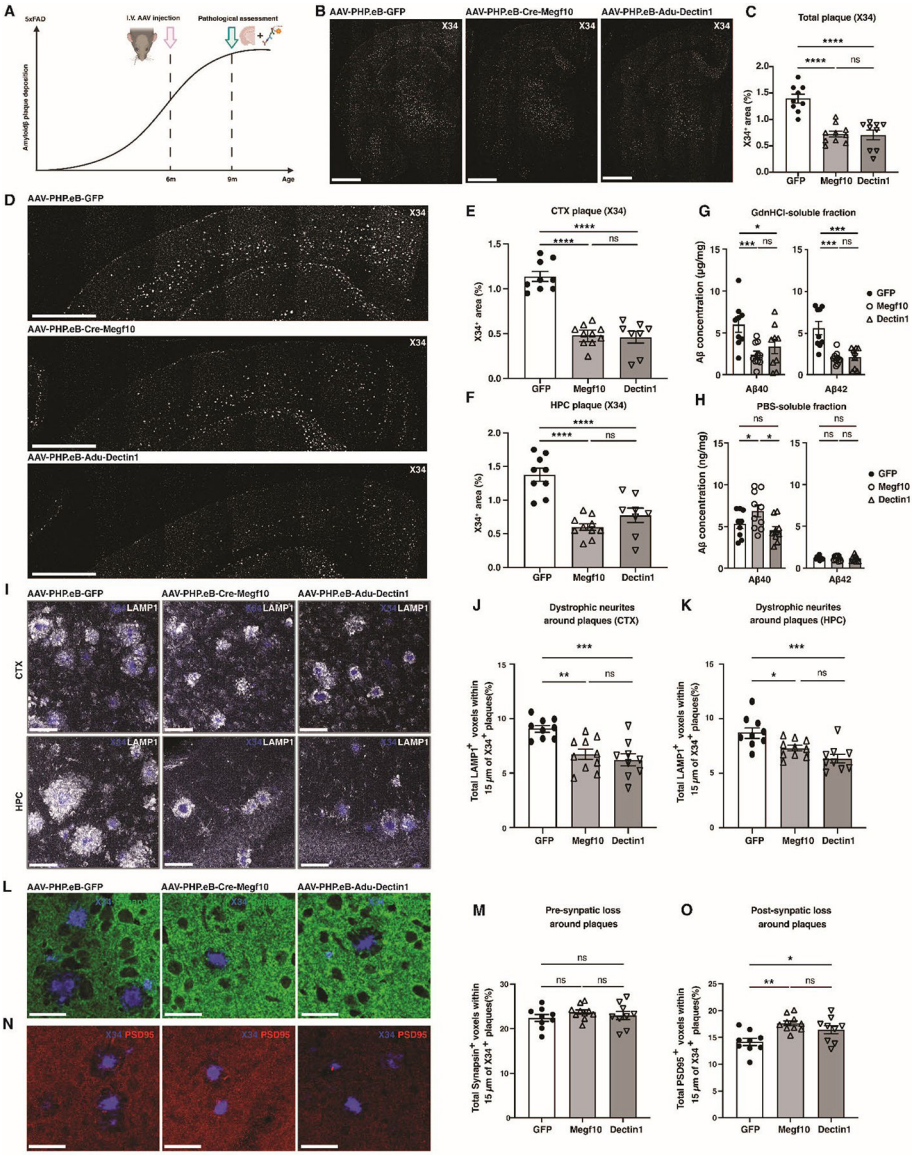

Fig. 2. One-time late timepoint AAV-CARA treatment reduces amyloidosis and amyloid-associated pathology *in vivo*.

(A) Experimental timeline for AAV injection and pathological assessment in 5xFAD mice post plaque formation. (B) Representative X34 staining of amyloid plaques in coronal brain sections. Scale bars: 1000 μm. (C) Quantification of total $X34^+$ plaque area in coronal sections. (D) Representative X34 staining of amyloid plaques in cortical sections from mice at 9 months of age, injected with AAV-PHP.eB -GFP, AAV-PHP.eB-Crene-Megf10, or AAV-PHP.eB-Adu-Dectin1. Scale bars: 1000 μm. (E and F) Quantification of $X34^+$ plaque area in cortex (E) and hippocampus (F). (G and H) ELISA results of Aβ40/42 in the GdnHCl soluble (G) or PBS soluble (H) fractions from cortical tissues of treated 5xFAD mice at 9 months of age. (I) Representative confocal images of $X34^+$ (blue) plaques and LAMP1 (white) staining in cortex and hippocampus. Scale bars: 30 μm. (J and K) Quantification of total $LAMP1^+$ voxels within 15μm around $X34^+$ plaques (%) in the cortex (J) or hippocampus (K) of treated 5xFAD mice at 9 months of age. (L) Representative

images and (M) quantification of total Synapsin^{+} voxels (green) within 15μm around X34^{+} plaques (%) in the cortex of treated 5xFAD mice at 9 months of age. (N) Representative images and (O) quantification of total PSD95^{+} voxels (red) within 15μm around X34^{+} plaques (%) in the cortex of treated 5xFAD mice at 9 months of age. Scale bars: 30 μm. Data in D, E, G, H, J, K, M, O are presented as mean ± SEM. N=9 for GFP, N=10 for Megf10, and N=9 for Dectin1. Statistical significance was calculated using one-way ANOVA with either Dunnett correction or Tukey correction for multiple comparison: *P < 0.05, **P < 0.01, ***P < 0.001, ****P < 0.0001, ns: not significant.

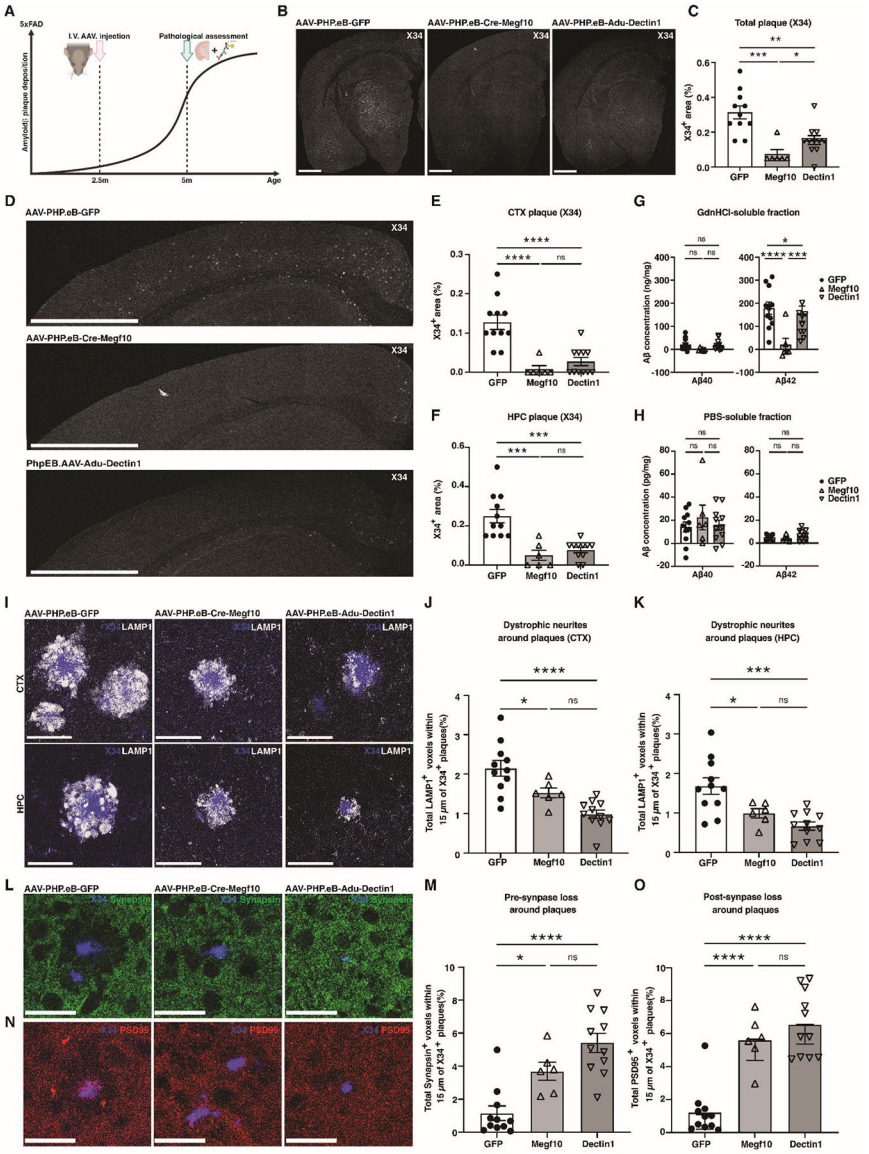

Fig. 3. One-time early AAV-CARA treatment prevents amyloid plaque formation and amyloid-associated pathology *in vivo*.

(A) Experimental timeline for AAV injection and pathological assessment in 5xFAD mice prior to plaque formation. (B) Representative X34 staining of amyloid plaques in coronal brain sections. Scale bars: 1000 μm. (C) Quantification of total $X34^+$ plaque area (%) in coronal sections. (D) Representative X34 staining of amyloid plaques in cortical sections from mice injected with AAV-PHP.eB -GFP, AAV-PHP.eB -Crene-Megf10, or AAV-PHP.eB-Adu-Dectin1 at 5 months of age. Scale bars: 1000 μm. (E and F) Quantification of $X34^+$ plaque area in cortex (E) and hippocampus (F). (G and H) ELISA results of Aβ40/42 in the GdnHCl soluble (G) or PBS soluble (H) fractions from cortical tissues of treated 5xFAD mice at 5 months of age. (I) Representative confocal images of $X34^+$ (blue) plaques and LAMP1 (white) staining in cortex and hippocampus. Scale bars: 30 μm. (J and K) Quantification of total $LAMP1^+$ voxels within 15μm around $X34^+$ plaques (%) in the cortex (J) or hippocampus (K) of treated 5xFAD mice at 5 months of age. (L) Representative

images and (M) quantification of total Synapsin^{+} voxels (green) within 15μm around X34^{+} plaques (%) in the cortex of treated 5xFAD mice at 5 months of age. (N) Representative images and (O) quantification of total PSD95^{+} voxels (red) within 15 μm around X34^{+} plaques (%) in the cortex of treated 5xFAD mice at 5 months of age. Scale bars: 30 μm. Data in C, E-H, J, K, M, O are presented as mean ± SEM. N=11 for GFP, N=6 for Megf10, and N=11 for Dectin1. Statistical significance was calculated using one-way ANOVA with either Dunnett correction or Tukey correction for multiple comparison: *P < 0.05, **P < 0.01, ***P < 0.001, ****P < 0.0001, ns: not significant.

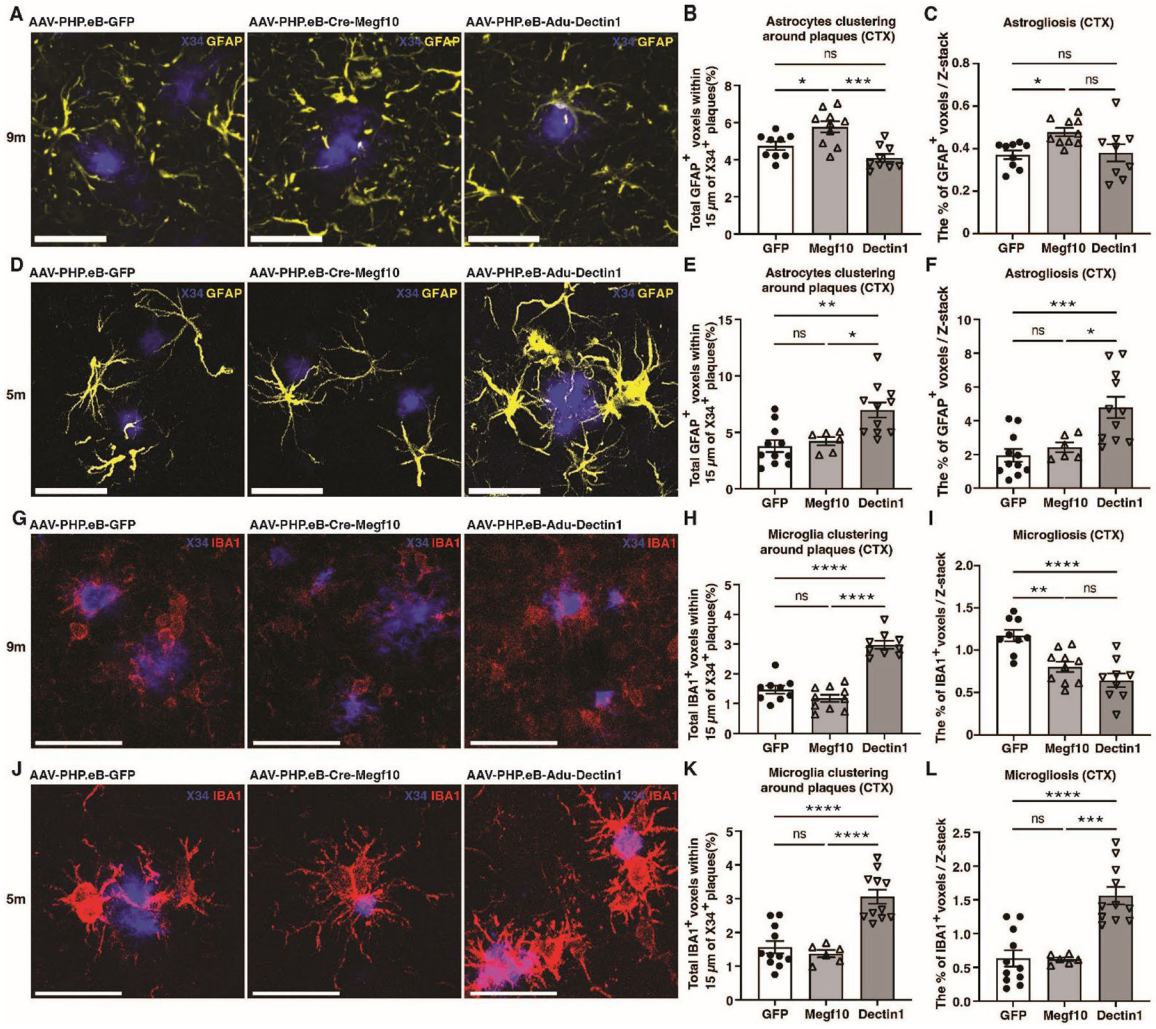

Fig. 4. Differential glial cell responses in the late CARA treatment and the early CARA prevention treatment.

(A) Representative images, (B) quantification of the percentage of GFAP$^+$ voxels within 15μm around X34$^+$ plaques (%) and (C) quantification of the percentage of total GFAP$^+$ volumes per Z-stack volume of interest (ROI) in the cortex of treated 5xFAD mice at 9 months of age. Scale bars: 30 μm. (D) Representative images, (E) quantification of the percentage of GFAP$^+$ voxels within 15μm around X34$^+$ plaques (%) and (F) quantification of the percentage of total GFAP$^+$ volumes per Z-stack volume of interest (ROI) in the cortex of treated 5xFAD at 5 months of age. Scale bars: 30 μm. (G) Representative images, (H) quantification of the percentage of IBA1$^+$ voxels within 15μm around X34$^+$ plaques (%) and (I) quantification of the percentage of total IBA1$^+$ volumes per Z-stack volume of interest (ROI) in the cortex of treated 5xFAD mice at 9 months of age. Scale bars: 30 μm. (J) Representative images, (K) quantification of the percentage of IBA1$^+$ voxels within 15μm around X34$^+$ plaques (%) and (L) quantification of the percentage of total IBA1$^+$ volumes per Z-stack volume of interest (ROI) in the cortex of treated 5xFAD at 5 months of age. Scale bars: 30 μm. Data in B&C, E&F, H&I, K&L are presented as mean ± SEM. N=9 for GFP, N=10 for Megf10, and N=9 for Dectin1 at 9 months; N=11 for GFP, N=6 for Megf10,

and N=11 for Dectin1 at 5 months. Statistical significance was calculated using one-way ANOVA with Tukey correction for multiple comparison: *P < 0.05, **P < 0.01, ***P < 0.001, ****P < 0.0001, ns: not significant.

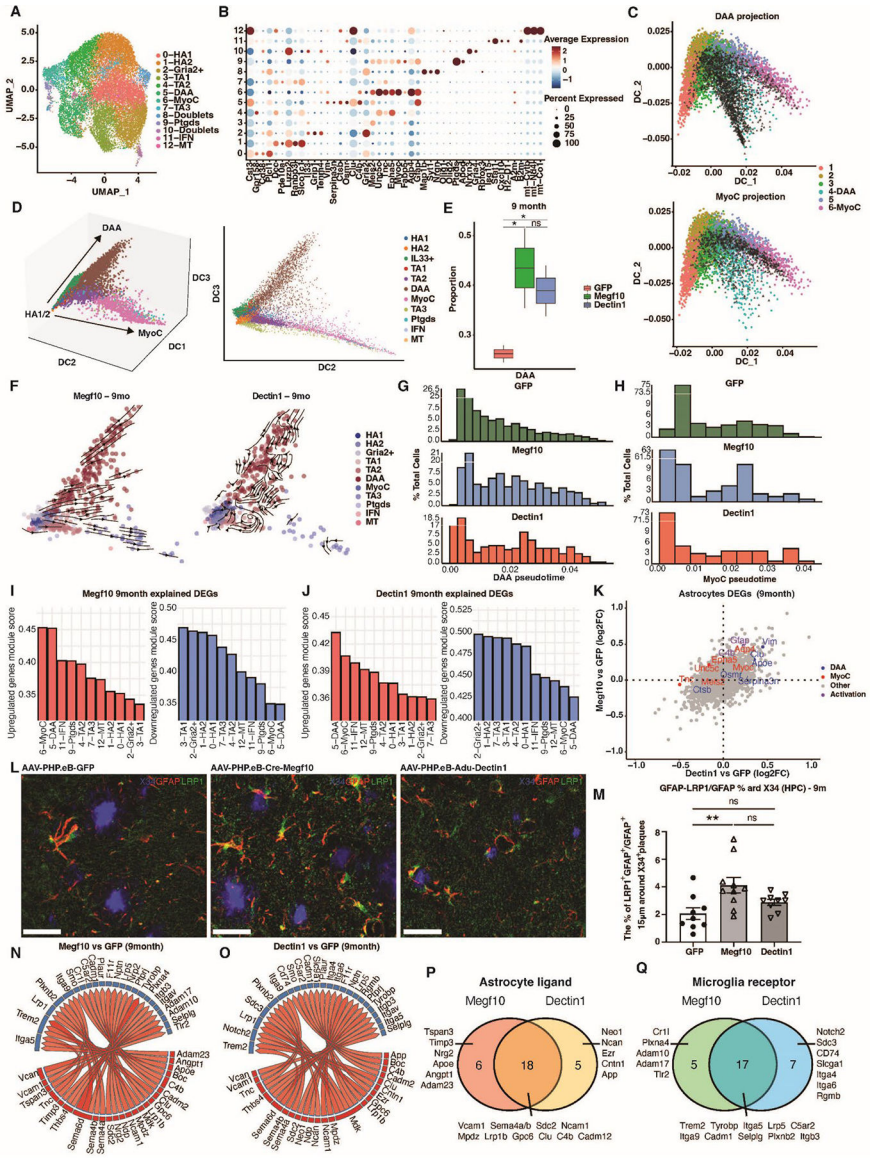

Figure 5. snRNA-seq reveals distinct alterations in astrocyte subpopulations by CAR-A treatment.

(A and B) Diversity of hippocampal astrocytes resolved by snRNA-seq. (A) UMAP of hippocampal astrocyte subsets after subclustering from the total dataset (as in Supplementary Figure 8A; n = 18,492 nuclei). (B) Dot plot of marker genes for astrocyte subclusters. (C) Projection of cluster 5 - DAA (top) and cluster 6 - MyoC astrocyte (bottom) onto diffusion map of snRNA-seq data from Habib et al. Colored dots: nuclei from Habib et al., black dots: nuclei from the present study. (D) 3D (left) and 2D (right) diffusion map embeddings of astrocyte subclusters (as in Figure 5A following exclusion of doublet clusters; total of 17,936 nuclei). Diffusion components 2 and 3 were used for the 2D embedding as they best recapitulate the differentiation trajectories. (E) Proportions of disease-associated astrocytes in GFP, Crene-Megf10, or Adu-Dectin1-treated groups at 9 months old. *: statistically credible change by scCoda. (F) RNA velocity stream plot on 2D diffusion map embeddings of Megf10 and Dectin1 astrocyte subsets at 9 months

old (n = 607 and 460 nuclei, respectively). (G and H) Histogram of astrocyte distribution along pseudotime for DAA (G) and MyoC (H) trajectories at 9 months old. (I and J) Bar plot showing module scores of upregulated (left) and downregulated (right) genes in each astrocyte subcluster for Crene-Megf10 vs GFP (I) or Adu-Dectin1 vs GFP (J) at 9 months old. Related to Supplementary Figure 8D–F. (K) Scatter plot of differentially expressed genes in astrocytes for Crene-Megf10 vs GFP and Adu-Dectin1 vs GFP at 9 months old. Representative genes are highlighted in color. (L) Representative images and (M) quantification of the percentage of $GFAP^+/LRP1^+$ voxels within $GFAP^+$ astrocytes (%) 15μm around $X34^+$ plaque in the hippocampus of treated 5xFAD mice at 9 months of age. Scale bars: 30 μm. (N and O) Circos plot displaying the top 30 upregulated ligand-receptor interactions in Crene-Megf10 (N) or Adu-Dectin1 (O) compared with GFP at 9 months old. Red: astrocytes; Blue: microglia. (P and Q) Pie graphs of overlapped gene analysis in the ligand-receptor interactions from astrocytic ligands (P) to microglial receptors (Q). HA: homeostatic astrocytes. TA: transitional astrocytes. DAA: disease-associated astrocytes. IFN: interferon-responsive astrocytes. DEGs: differentially expressed genes. Data in M are presented as mean ± SEM. N=9 for GFP, N=10 for Megf10, and N=9 for Dectin1. Statistical significance was calculated using one-way ANOVA with Tukey correction for multiple comparison: *P < 0.05, **P < 0.01, ***P < 0.001, ****P < 0.0001, ns: not significant.

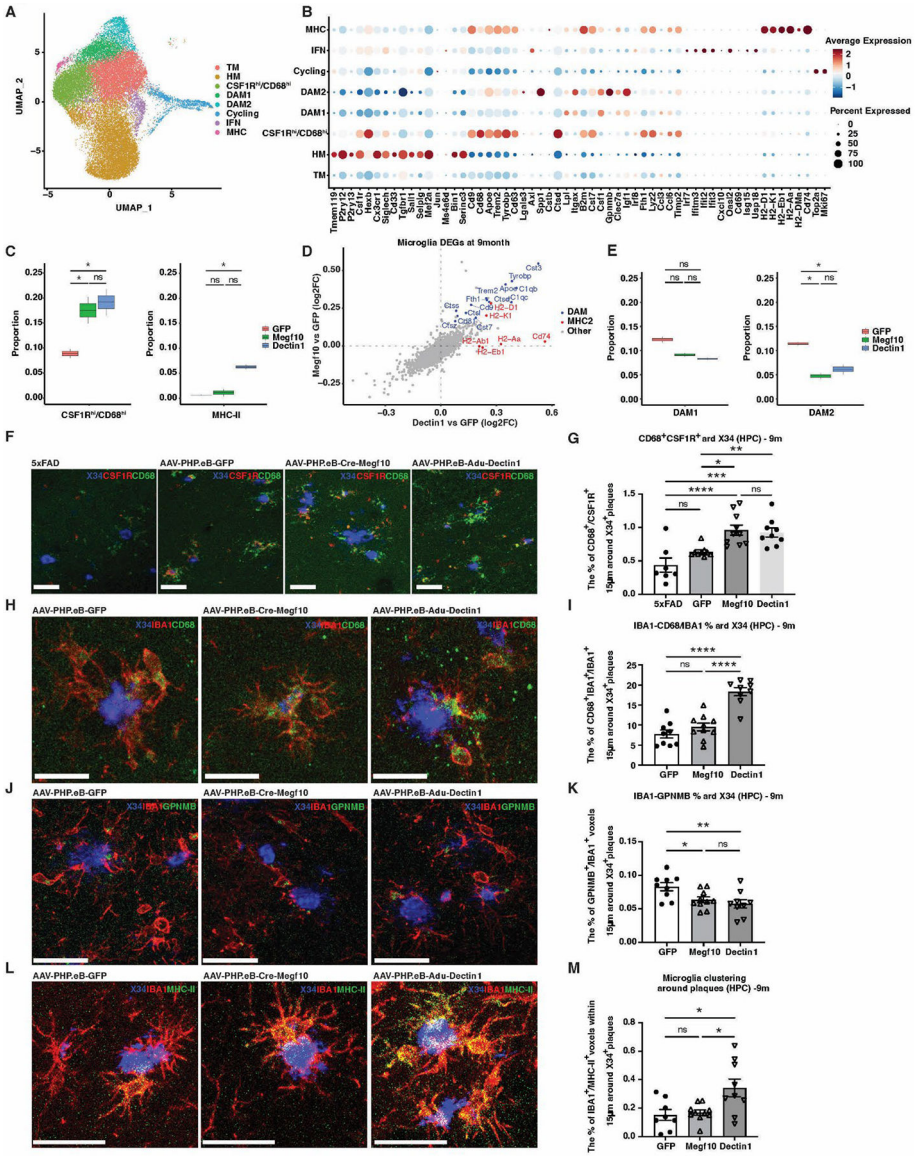

Figure 6. CAR-A treatment induces unique microglial responses between Crene-Megf10 and Adu-Dectin1 when compared to GFP controls.

(A and B) Microglia subsets resolved by snRNA-seq. (A) UMAP of microglia subsets following integration of the 5- and 9-month-old timepoints (n = 31,581 nuclei). (B) Dot plot of marker genes for each microglia subset. (C) Box plot showing the proportion of $CD68^{hi}$ (left) and MHC-II (right) microglia subsets at 9 months old. (D) Scatter plot of differentially expressed genes in microglia comparing Crene-Megf10 vs GFP and Adu-Dectin1 vs GFP at 9 months old. Blue: DAM genes. Red: MHC-II genes. (E) Box plot showing the proportions of DAM1 (left) and DAM2 (right) in GFP, Crene-Megf10, and Adu-Dectin1 groups at 9 months old. (F) Representative images and (G) quantification of the percentage of $CSF1R^{+}$/$CD68^{+}$ voxels within 15μm around $X34^{+}$ plaque in the hippocampus of treated 5xFAD mice at 9 months of age. Scale bars: 30 μm. (H) Representative images and (I) quantification of the percentage of $CD68^{+}$/$IBA1^{+}$ voxels within $IBA1^{+}$ microglia (%) 15μm around $X34^{+}$ plaque in the hippocampus of treated 5xFAD mice at 9 months of age. Scale bars: 30

μm. (J) Representative images and (K) quantification of the percentage of $GPNMB^+/IBA1^+$ voxels within $IBA1^+$ microglia (%) 15μm around $X34^+$ plaque in the hippocampus of treated 5xFAD mice at 9 months of age. Scale bars: 30 μm. (L) Representative images and (M) quantification of the percentage of $MHC\text{-}II^+/IBA1^+$ voxels within $IBA1^+$ microglia (%) 15μm around $X34^+$ plaque in the hippocampus of treated 5xFAD mice at 9 months of age. Scale bars: 30 μm. TM: transitional microglia. HM: homeostatic microglia. DAM: disease-associated microglia. Data in G, I, K, M are presented as mean ± SEM. N=7 for 5xFAD in G, N=9 for GFP, N=10 for Megf10, and N=9 for Dectin1. Statistical significance was calculated using one-way ANOVA with Tukey correction for multiple comparison: *P < 0.05, **P < 0.01, ***P < 0.001, ****P < 0.0001, ns: not significant.